

RESEARCH ARTICLE

10.1002/2015WR017723

Correlation equations for average deposition rate coefficients of nanoparticles in a cylindrical pore

N. Seetha¹, S. Majid Hassanizadeh², M. S. Mohan Kumar³, and Amir Raouf²

¹Department of Civil Engineering, Indian Institute of Science, Bangalore, India, ²Department of Earth Sciences, Utrecht University, Utrecht, Netherlands, ³Department of Civil Engineering and Indo-French Cell for Water Sciences, Indian Institute of Science, Bangalore, India

Key Points:

- Expressions for mass transfer rate coefficients between bulk and wall regions
- Deposition rate coefficients follow a power law relation with pore-scale parameters
- Correlation equations qualitatively agree with colloid filtration theory

Correspondence to:

M. S. Mohan Kumar,
msmk@civil.iisc.ernet.in

Citation:

Seetha, N., S. Majid Hassanizadeh, M. S. Mohan Kumar, and A. Raouf (2015), Correlation equations for average deposition rate coefficients of nanoparticles in a cylindrical pore, *Water Resour. Res.*, 51, 8034–8059, doi:10.1002/2015WR017723.

Received 20 JUN 2015

Accepted 4 SEP 2015

Accepted article online 7 SEP 2015

Published online 12 OCT 2015

Abstract Nanoparticle deposition behavior observed at the Darcy scale represents an average of the processes occurring at the pore scale. Hence, the effect of various pore-scale parameters on nanoparticle deposition can be understood by studying nanoparticle transport at pore scale and upscaling the results to the Darcy scale. In this work, correlation equations for the deposition rate coefficients of nanoparticles in a cylindrical pore are developed as a function of nine pore-scale parameters: the pore radius, nanoparticle radius, mean flow velocity, solution ionic strength, viscosity, temperature, solution dielectric constant, and nanoparticle and collector surface potentials. Based on dominant processes, the pore space is divided into three different regions, namely, bulk, diffusion, and potential regions. Advection-diffusion equations for nanoparticle transport are prescribed for the bulk and diffusion regions, while the interaction between the diffusion and potential regions is included as a boundary condition. This interaction is modeled as a first-order reversible kinetic adsorption. The expressions for the mass transfer rate coefficients between the diffusion and the potential regions are derived in terms of the interaction energy profile. Among other effects, we account for nanoparticle-collector interaction forces on nanoparticle deposition. The resulting equations are solved numerically for a range of values of pore-scale parameters. The nanoparticle concentration profile obtained for the cylindrical pore is averaged over a moving averaging volume within the pore in order to get the 1-D concentration field. The latter is fitted to the 1-D advection-dispersion equation with an equilibrium or kinetic adsorption model to determine the values of the average deposition rate coefficients. In this study, pore-scale simulations are performed for three values of Péclet number, $Pe = 0.05, 5, \text{ and } 50$. We find that under unfavorable conditions, the nanoparticle deposition at pore scale is best described by an equilibrium model at low Péclet numbers ($Pe = 0.05$) and by a kinetic model at high Péclet numbers ($Pe = 50$). But, at an intermediate Pe (e.g., near $Pe = 5$), both equilibrium and kinetic models fit the 1-D concentration field. Correlation equations for the pore-averaged nanoparticle deposition rate coefficients under unfavorable conditions are derived by performing a multiple-linear regression analysis between the estimated deposition rate coefficients for a single pore and various pore-scale parameters. The correlation equations, which follow a power law relation with nine pore-scale parameters, are found to be consistent with the column-scale and pore-scale experimental results, and qualitatively agree with the colloid filtration theory. These equations can be incorporated into pore network models to study the effect of pore-scale parameters on nanoparticle deposition at larger length scales such as Darcy scale.

1. Introduction

Understanding processes responsible for colloid transport and deposition in porous media is crucial for the adequate prediction of the movement of pathogens (viruses, bacteria, and protozoa), engineered nanoparticles, and colloid-facilitated transport of contaminants. Colloid deposition involves two sequential steps: transport to the grain surface and attachment. The transport of colloids to the pore surface is dominated by advection and diffusion, while the attachment is controlled by colloid-soil interaction forces, which operate at short separation distances [Elimelech and O'Melia, 1990]. Colloid deposition depends on a number of factors such as the flow velocity [Hijnen et al., 2005; Keller et al., 2004; Li et al., 2005; May et al., 2012; Tong and Johnson, 2006; Tosco et al., 2012; Zhang, 2013], solution chemistry [Bergendahl and Grasso, 1999; Johnson et al., 2007a; Knappett et al., 2008; Loveland et al., 1996; Sadeghi et al., 2011; Tufenkji and Elimelech, 2005], surface characteristics of colloids and grain [Chu et al., 2001; Johnson et al., 1996; Li et al., 2008; Tufenkji and

Elimelech, 2005; Zhang et al., 2014; Zhuang and Jin, 2003; Zhuang et al., 2005], grain size and shape [Knappett et al., 2008; Li et al., 2008; Shen et al., 2008; Tong and Johnson, 2006], colloid size [Keller et al., 2004; Shen et al., 2008; Tong and Johnson, 2006; Wang et al., 2012; Zhuang et al., 2005], temperature [Chrysikopoulos and Aravantinou, 2014; Syngouna and Chrysikopoulos, 2010; Yan et al., 2015], and water content [Torkzaban et al., 2006a, 2006b; Zhang et al., 2013].

Colloid attachment to the grain surface is usually described using the “clean-bed” filtration model, the Colloid Filtration Theory (CFT) [Yao et al., 1971]. According to CFT, the attachment of particles to the grain surface is assumed to be described by a first-order irreversible kinetic model, with the attachment rate coefficient given as

$$k_{att(D)} = \frac{3(1-\theta)}{2d_c} U \alpha \eta_0 \quad (1)$$

where $k_{att(D)}$ is the Darcy-scale attachment rate coefficient, θ is the porosity, d_c is the average grain diameter, U is the pore water velocity, α is the attachment efficiency, and η_0 is the single collector contact efficiency without inclusion of the electric double layer interaction. The single collector efficiency is the ratio of the rate at which particles strike the collector to the rate at which particles flow toward the collector [Yao et al., 1971]. It accounts for the effect of physical factors involved in colloid deposition and is calculated as the sum of contributions from three individual mechanisms, namely, Brownian diffusion, interception, and sedimentation. The collector efficiency can be determined using the correlation equations available in the literature [Ma et al., 2013; Messina et al., 2015; Nelson and Ginn, 2011; Rajagopalan and Tien, 1976; Tufenkji and Elimelech, 2004a; Yao et al., 1971]. These correlation equations were developed by numerically solving the colloid transport equation in an idealized porous medium over a wide range of parameter values and regressing the numerical results against the input parameters. The correlation equations differ in the underlying physical mechanisms considered in modeling the colloid transport to the grain surface. The attachment efficiency, α , representing the favorability of the surface for deposition, is the ratio of the collisions resulting in attachment to the total number of collisions between colloids and the collector. It accounts for the effect of system chemistry on colloid attachment and is assumed to be independent of system hydrodynamics. Experimental studies indicate that the particle deposition behavior is in good agreement with CFT (equation (1)) under conditions favorable for deposition ($\alpha = 1$) [Elimelech and O'Melia, 1990; Nelson and Ginn, 2011; Rajagopalan and Tien, 1976; Tufenkji and Elimelech, 2004a, 2005]. But, CFT is generally observed to breakdown under unfavorable conditions (i.e., $\alpha < 1$). This is because CFT does not include effects such as the deposition onto the secondary energy minimum, surface charge heterogeneities, surface roughness, and deposition at grain-grain contacts [Elimelech and O'Melia, 1990; Hahn and O'Melia, 2004; Johnson et al., 2007a, 2007b; Shen et al., 2007; Tufenkji and Elimelech, 2004b, 2005].

Attachment efficiency, α , can be calculated using available theoretical or empirical expressions in the literature. For example, α can be estimated theoretically from Derjaguin-Landau-Verwey-Overbeek (DLVO) theory [Derjaguin and Landau, 1941; Verwey and Overbeek, 1948] using two approaches: (1) interaction force boundary layer (IFBL) approach [Spielman and Friedlander, 1974] and (2) Maxwell approach [Hahn and O'Melia, 2004; Shen et al., 2007, 2010]. IFBL approach predicts particle deposition rate in the primary minimum in the presence of repulsive energy barrier and neglects particle accumulation in the secondary minimum. However, experimental attachment efficiencies (obtained from equation (1), using theoretical value of η_0 and the fitted value of $k_{att(D)}$ [Tufenkji and Elimelech, 2004b]) were found to be orders of magnitude greater than the values predicted by IFBL approach in the presence of repulsive energy barrier [Elimelech and O'Melia, 1990; Hahn and O'Melia, 2004; Shen et al., 2007]. Although theoretical attachment efficiency is assumed to be independent of system hydrodynamics, studies have shown that the experimental attachment efficiency decreases with increasing flow velocity [Anders and Chrysikopoulos, 2005; Johnson et al., 2007a; Keller et al., 2004]. Also, in contrast to the theory, the experimental attachment efficiency is found to be insensitive to the particle size. The arguments for these deviations are that in IFBL approach certain important factors, such as the deposition in the secondary minimum, grain roughness and shape, straining, surface charge heterogeneity of the collector, and hydrodynamic forces, are not accounted for. Shen et al. [2007] used Maxwell approach to estimate particle attachment efficiency under unfavorable conditions by considering deposition at both primary and secondary minima. They found that the experimental attachment efficiencies for small colloids (smaller than 30 nm) are in good agreement with the Maxwell

predictions within 1–1.5 orders of magnitude. But, for large colloids, the experimental attachment efficiencies are slightly smaller than Maxwell predictions (within 1.5 orders of magnitude), maybe because of the assumption that the attachment efficiency is independent of system hydrodynamics, which would be more pronounced for large colloids [Johnson *et al.*, 2007a; Keller *et al.*, 2004; Shen *et al.*, 2007, 2010]. Later, Shen *et al.* [2010] modified the model of Shen *et al.* [2007] to predict attachment efficiency under unfavorable conditions by incorporating the effect of system hydrodynamics on colloid deposition at both primary and secondary minima. This was accomplished via comparison of the adhesive and hydrodynamic torques acting on the colloids deposited at both primary and secondary minima [Shen *et al.*, 2010]. However, the escape of secondary-minimum-deposited colloids to bulk suspension was not considered. The predictions from this model were found to be in better agreement with the experimental attachment efficiencies as compared to the IFBL approach and the Maxwell approach followed by Shen *et al.* [2007]. Though the Maxwell approach could predict reasonably well the particle deposition under unfavorable conditions with the incorporation of torque balance [Shen *et al.*, 2010], a quantitative relationship between the attachment efficiency and the various factors affecting it is still not available. Chang and Chan [2008] developed a correlation equation for α under unfavorable conditions using a triangular network model and adopting the Brownian dynamic simulation method. There, α is calculated as the sum of the contributions from four deposition mechanisms: Brownian diffusion, interception, sedimentation, and DLVO interactions. Though not mechanistically based, empirical correlation expressions relating the experimental attachment efficiency to the various dimensionless parameters affecting it are available in the literature [Bai and Tien, 1999; Elimelech, 1992; Park *et al.*, 2012]. However, their applicability is limited to the range of experimental conditions under which the correlation equations are developed.

Colloid detachment is significant under unfavorable conditions for deposition and may increase the colloid transport distance. It is observed to depend on flow velocity [Bergendahl and Grasso, 2000; Li *et al.*, 2005; Tong and Johnson, 2006], solution chemistry [Bergendahl and Grasso, 1999; Compere *et al.*, 2001; Johnson *et al.*, 2007a; Li *et al.*, 2004, 2005], colloid size [Tong and Johnson, 2006; Wang *et al.*, 2012], and grain size. Unlike colloid attachment, colloid detachment is not considered in CFT, and there is no predictive model available to estimate colloid detachment quantitatively.

A comprehensive mechanistic approach is needed to better understand the colloid deposition in porous media. Pore-scale modeling and the subsequent upscaling to Darcy scale offers a reliable tool to study colloid transport in porous media and can be used to derive quantitative relationships between the Darcy-scale parameters and various pore-scale parameters. In this study, we derive correlation equations for the average deposition rate coefficients of nanoparticles (radii ≤ 100 nm) in a cylindrical pore in terms of nine pore-scale parameters: the pore radius, nanoparticle radius, mean flow velocity, solution ionic strength, fluid viscosity, temperature, fluid dielectric constant, and nanoparticle and collector surface potentials. Such correlation equations are particularly appropriate to be incorporated into pore network models [e.g., Raouf *et al.*, 2010] to continue upscaling nanoparticle transport to the Darcy scale. The sequence of steps that we have followed in deriving the correlation expressions are: (1) simulating the transport of nanoparticles in a cylindrical pore for a range of values of pore-scale parameters, (2) averaging the resulting nanoparticle concentration over a moving averaging volume to get the 1-D concentration field, (3) fitting the 1-D nanoparticle concentration field obtained from the pore-scale model against 1-D advection-dispersion equation, with an equilibrium or kinetic adsorption model, in order to determine the values of pore-averaged deposition rate coefficients, and (4) developing correlation equations for the average nanoparticle deposition rate coefficients at pore scale by performing a multiple-linear regression analysis between the pore-averaged deposition rate coefficients and the nine pore-scale parameters mentioned above.

2. Nanoparticle Transport in a Cylindrical Pore

2.1. Mathematical Model

The mathematical model used in this study to simulate nanoparticle transport at the pore scale is obtained through modifying the model developed by Seetha *et al.* [2014], who simulated virus-sized colloid transport in a cylindrical pore at steady state by solving the full transport equations accounting for advection, diffusion, hydrodynamic wall effects, and colloid-collector surface interactions. Figure 1 represents a cylindrical pore with radius R and length L through which a dilute suspension of spherical nanoparticles with radius a

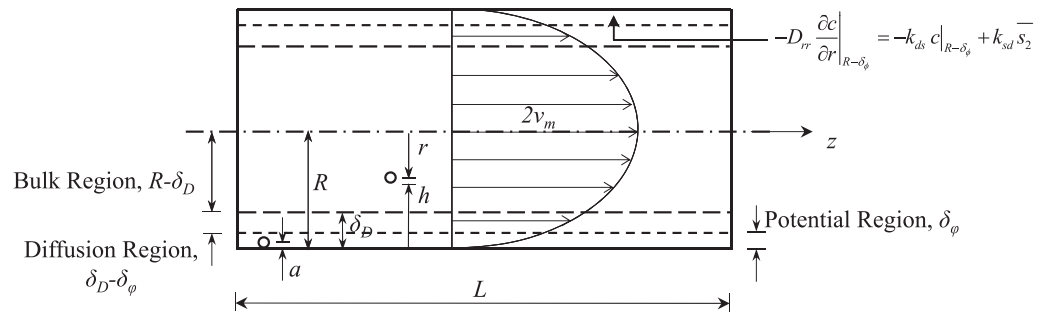


Figure 1. Conceptual representation of a pore.

is flowing. Seetha et al. [2014] divided the pore space into three different regions, namely, bulk, diffusion, and potential regions, based on the dominant processes acting in each of these regions (Figure 1). Nanoparticle transport is governed by advection and diffusion in the bulk region, whereas nanoparticle mobility due to diffusion is reduced by hydrodynamic wall effects in the diffusion region. Nanoparticle-collector surface forces dominate the transport in the potential region where nanoparticle deposition occurs. In Figure 1, δ_D denotes the position of the interface between the bulk and diffusion regions, and δ_ϕ the position of the interface between the diffusion and potential regions, both being measured from the surface of the pore. There, h denotes the separation distance between the nanoparticle and the wall. The entire pore is a single continuous domain with concentration being continuous across the three different regions. Seetha et al. [2014] further assumed that (1) the flow is fully developed, laminar and at steady state, (2) particles in the potential region are effectively immersed in a simple shear flow where the hydrodynamic wall effects are significant, (3) the suspension is dilute and stable and, hence, interactions between the particles can be neglected, (4) particles are sufficiently small such that the gravitational and lift forces are neglected [Song and Elimelech, 1993; Wood et al., 2004; Yao et al., 1971], and (5) the particles and the collector surface are negatively charged.

The nanoparticle transport in the bulk and diffusion regions is described by the following two advection-diffusion equations, respectively [Seetha et al., 2014]

$$\frac{\partial c}{\partial t} = D_\infty \left(\frac{\partial^2 c}{\partial r^2} + \frac{1}{r} \frac{\partial c}{\partial r} \right) + D_\infty \frac{\partial^2 c}{\partial z^2} - v_1 \frac{\partial c}{\partial z}; \quad 0 \leq r \leq R - \delta_D \quad (2)$$

$$\frac{\partial c}{\partial t} = \frac{\partial}{\partial r} \left(D_{rr} \frac{\partial c}{\partial r} \right) + \frac{1}{r} D_{rr} \frac{\partial c}{\partial r} + \frac{\partial}{\partial z} \left(D_{zz} \frac{\partial c}{\partial z} \right) - v_1 \frac{\partial c}{\partial z}; \quad R - \delta_D \leq r \leq R - \delta_\phi \quad (3)$$

where c represents the nanoparticle number concentration, D_∞ is the nanoparticle bulk diffusion coefficient given by Stoke-Einstein relation as $D_\infty = (k_B T / 6\pi\mu a)$, k_B is the Boltzmann constant, T is the absolute temperature, μ is the dynamic viscosity of water, v_1 is the steady state flow velocity given by Poiseuille equation as $v_1 = 2v_m [1 - (r/R)^2]$, and v_m is the mean pore water velocity. $D_{rr}(r)$ and $D_{zz}(r)$ are, respectively, the position-dependent particle diffusion coefficients in the radial and axial directions affected by hydrodynamic wall effects, and are given in section A1. δ_D is taken as the normal distance from the wall at which $D_{rr} = 0.99D_\infty$ [Wood et al., 2004], which is found to be $\delta_D \approx 100a$ [Song and Elimelech, 1993].

There is exchange of particles between diffusion and potential regions in the radial direction. The rate expression for this particle flux is [Song and Elimelech, 1993; Wood et al., 2004]

$$J_h(z) = -D_{rr} \frac{dc}{dh} - \frac{D_{rr}}{k_B T} \frac{d\Phi}{dh} c \quad (4)$$

where Φ is the total interaction energy between the particle and the grain surface calculated using DLVO theory. Figure 2 shows three different types of interaction energy profile that can exist between the nanoparticle and the grain surface. Type-I energy profile is characterized by two minima separated by an energy barrier: a primary minimum existing closer to the surface and a secondary minimum existing far away from

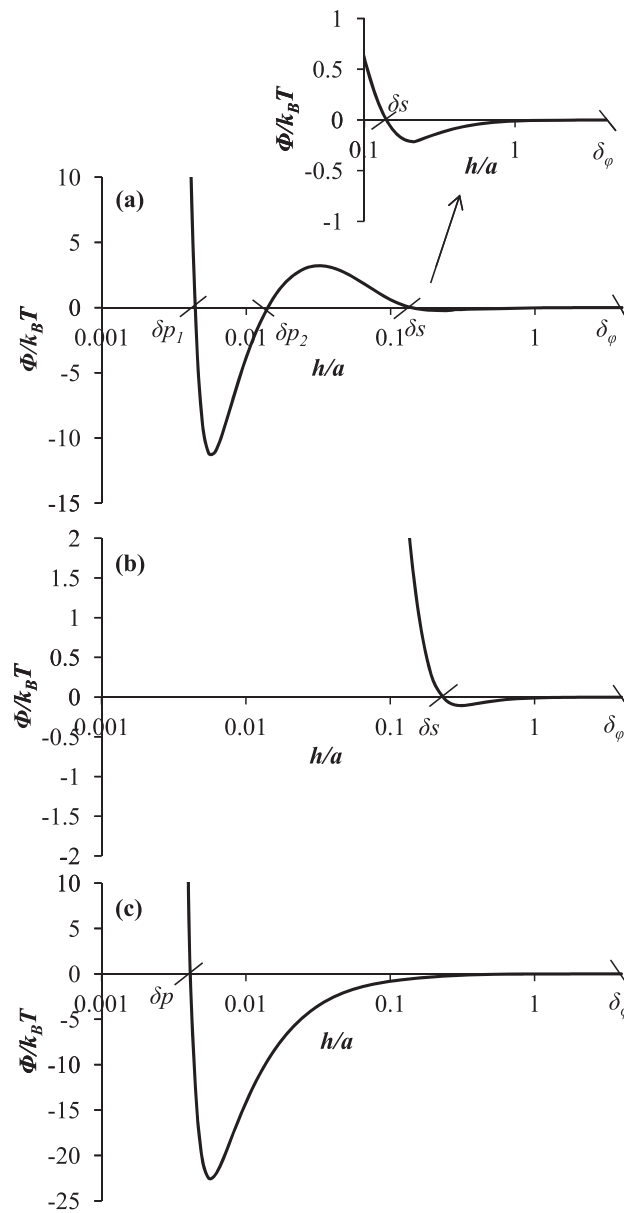


Figure 2. Types of interaction energy profiles: (a) Type-I (the interaction energy profile near the secondary minimum is shown in the inset), (b) Type-II, and (c) Type-III energy profiles.

the surface. Type-II energy profile is characterized by a secondary minimum (and no primary minimum). Type-III energy profile is characterized by a single minimum (a primary minimum) existing closer to the surface. Seetha et al. [2014] solved the complete transport equation in the potential region, by accounting for advection, diffusion, hydrodynamic wall effects, and colloid-collector interactions (section A2). However, the need for very fine computational mesh in the potential region, to capture the shape and peaks in the interaction energy profile accurately, causes increased computational times. As the potential region is very thin (a few hundreds of nanometers), one may average the processes over the thickness of this layer. We build upon the approach of Ruckenstein and Prieve [1973] and Spielman and Friedlander [1974], who suggested that the effect of colloidal interaction forces on the rate of deposition of particles can be included in the form of boundary conditions for the convective-diffusion equation in the bulk region at the collector surface. Hence, the governing equation for nanoparticle distribution in the potential region (section A2) is averaged over the potential region in the radial direction, resulting in differential equations for particle accumulation in primary and secondary minimum regions. The resulting governing equations for a Type-I profile are as follows (refer to Figure 3a)

$$\frac{\partial \bar{s}_2}{\partial t} = -\bar{v}_2 f_2' \frac{\partial \bar{s}_2}{\partial z} + k_{ds} c|_{R-\delta_\phi} - k_{sd} \bar{s}_2 - k_{sp} \bar{s}_2 + k_{ps} \bar{s}_1 \quad (5a)$$

$$\frac{\partial \bar{s}_1}{\partial t} = k_{sp} \bar{s}_2 - k_{ps} \bar{s}_1 \quad (5b)$$

Here \bar{s}_1 [no. L^{-2}] and \bar{s}_2 [no. L^{-2}] are the average particle concentrations at primary and secondary minima, respectively, defined as $\bar{s}_1 = \int_{\delta p_1}^{\delta p_2} c(h) dh$ and $\bar{s}_2 = \int_{\delta s}^{\delta_\phi} c(h) dh$, δp_1 [L], δp_2 [L], and δs [L] are defined in Figure 2a, \bar{v}_2 is the average velocity of mobile particles in the secondary minimum region, k_{ds} [$L T^{-1}$] is the mass transfer rate coefficient corresponding to nanoparticle transport from diffusion region to the secondary minimum region, k_{sd} [T^{-1}] is the mass transfer rate coefficient corresponding to nanoparticle transport from secondary minimum region to the diffusion region, k_{sp} [T^{-1}] is the mass transfer rate coefficient corresponding to nanoparticle transport from secondary minimum region to the primary minimum region, and k_{ps} [T^{-1}] is the mass transfer rate coefficient corresponding to nanoparticle transport from primary minimum region to the secondary minimum region. We assume that a fraction, f_2' , of particles in the secondary minimum region is mobile in the longitudinal direction by advection. The particle velocity in the potential region is assumed to be given by [Song and Elimelech, 1993]

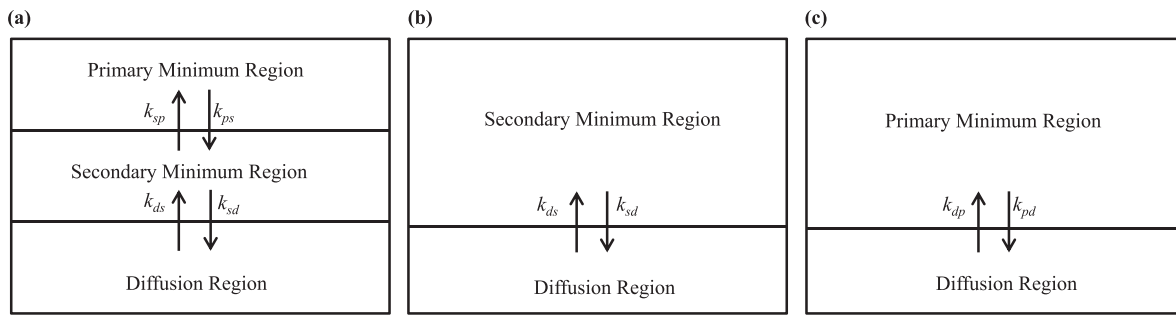


Figure 3. Mass transfer rate coefficients for nanoparticle deposition for (a) Type-I, (b) Type-II, and (c) Type-III energy profiles.

$$v_2(r) = f_3(r) \frac{4v_m(R-r)}{R} \tag{6}$$

where f_3 is the universal hydrodynamic correction function for the particle velocity along the wall in simple shear flow [Dahneke, 1974; Warszynski, 2000] and is given in section A1. δ_ϕ is taken as the distance from the wall at which $\Phi \ll 0.01k_B T$, so that the interaction energy becomes negligible in the diffusion region. The expressions for the mass transfer rate coefficients and f_2' are derived in terms of the interaction energy profile and is given in section 2.2.

Particle accumulation in the secondary minimum region for a Type-II energy profile is governed by the following equation (refer to Figure 3b)

$$\frac{\partial \bar{s}_2}{\partial t} = -\bar{v}_2 f_2' \frac{\partial \bar{s}_2}{\partial z} + k_{ds} c \Big|_{R-\delta_\phi} - k_{sd} \bar{s}_2 \tag{7}$$

The definitions for \bar{s}_2 , \bar{v}_2 , f_2' , k_{ds} , and k_{sd} are same as that for a Type-I energy profile.

The governing equation for particle accumulation in the potential region for a Type-III energy profile is (refer to Figure 3c)

$$\frac{\partial \bar{s}_1}{\partial t} = -\bar{v}_1 f_1' \frac{\partial \bar{s}_1}{\partial z} + k_{dp} c \Big|_{R-\delta_\phi} - k_{pd} \bar{s}_1 \tag{8}$$

where \bar{s}_1 [no. L^{-2}] is the average particle concentration at primary minimum defined as $\bar{s}_1 = \int_{\delta_\phi}^{\delta_\phi} c(h) dh$, δp [L] is defined in Figure 2c, \bar{v}_1 [LT^{-1}] is the average velocity of mobile particles in the potential region, f_1' is the fraction of particles in the primary minimum region that are mobile in the longitudinal direction by advection, k_{dp} [LT^{-1}] is the mass transfer rate coefficient for nanoparticle transport from diffusion region to the primary minimum region, and k_{pd} [T^{-1}] is the mass transfer rate coefficient for nanoparticle transport from primary minimum region to the diffusion region.

2.2. Mass Transfer Rate Coefficients and Torque Balance

In this section, we derive expressions for the mass transfer rate coefficients, k_{ds} , k_{sd} , k_{sp} , k_{ps} , k_{dp} , and k_{pd} in terms of the interaction energy profile. The expressions for the fraction of mobile particles in the secondary minimum, f_2' (for Type-I and Type-II energy profiles), and primary minimum, f_1' (for a Type-III energy profile) are derived by performing a balance of hydrodynamic and adhesive torques acting on particles in the potential region.

2.2.1. Expressions for Mass Transfer Rate Coefficients

The expressions for the mass transfer rate coefficients, k_{sp} and k_{ps} , for a Type-I energy profile were derived by Ruckenstein [1978]. Ruckenstein [1978] assumed that in the presence of an energy barrier, the relaxation time needed to reach equilibrium distribution at the primary and secondary minima of a Type-I energy profile is short compared to the time during which the concentration of the particles at the minima changes appreciably. Hence, a Boltzmann distribution ($J_h(z)=0$ in equation (4)) is valid for the concentration of particles in the secondary and primary minima. The resulting concentration distributions at the secondary (equation (9a)) and primary minima (equation (9b)) for a Type-I energy profile are

$$c(h) = \frac{\bar{s}_2 e^{-\Phi/k_B T}}{\int_{\delta_s}^{\delta_\phi} e^{-\Phi/k_B T} dh} \tag{9a}$$

$$c(h) = \frac{\bar{s}_1 e^{-\Phi/k_B T}}{\int_{\delta_{p1}}^{\delta_{p2}} e^{-\Phi/k_B T} dh} \tag{9b}$$

Expressions for the mass transfer rate coefficients, k_{sp} and k_{ps} , assuming quasi steady state conditions across the energy barrier (equation (4)), were derived as [Ruckenstein, 1978]

$$k_{sp} = \frac{1}{\int_{\delta_s}^{\delta_\phi} e^{-\Phi/k_B T} dh} \frac{1}{\int_{\delta_{p2}}^{\delta_s} \frac{e^{\Phi/k_B T}}{D(h)} dh} \quad k_{ps} = \frac{1}{\int_{\delta_{p1}}^{\delta_{p2}} e^{-\Phi/k_B T} dh} \frac{1}{\int_{\delta_{p2}}^{\delta_s} \frac{e^{\Phi/k_B T}}{D(h)} dh} \tag{10}$$

The expressions for the mass transfer rate coefficients, k_{ds} and k_{sd} , for a Type-I energy profile can be derived by equating the flux at the diffusion region-potential region interface

$$J_r(z) = -D \frac{dc}{dr} \Big|_{R-\delta_\phi} = D \frac{dc}{dh} \Big|_{R-\delta_\phi} + \frac{D}{k_B T} \frac{d\Phi}{dh} \Big|_{R-\delta_\phi} c \Big|_{R-\delta_\phi} \tag{11}$$

Substituting for $\frac{dc}{dh}$ from equation (9a) in equation (11), we obtain the following expression (equation (12)) for the flux at the diffusion region-potential region interface with the corresponding expressions for k_{ds} and k_{sd} as given in equation (13).

$$-D \frac{dc}{dr} \Big|_{R-\delta_\phi} = -k_{sd} \bar{s}_2 + k_{ds} c \Big|_{R-\delta_\phi} \tag{12}$$

$$k_{ds} = \frac{D \Big|_{\delta_\phi} \frac{d\Phi}{dh} \Big|_{\delta_\phi}}{k_B T} \quad k_{sd} = \frac{D \Big|_{\delta_\phi} \frac{d\Phi}{dh} \Big|_{\delta_\phi}}{\int_{\delta_s}^{\delta_\phi} e^{-\Phi/k_B T} dh} \frac{e^{-\Phi/k_B T} \Big|_{\delta_\phi}}{k_B T} \tag{13}$$

2.2.2. Torque Balance

Colloid immobilization on the grain surface depends on the pore structure, pore size, flow velocity, solution chemistry, colloid size, and surface roughness [Bergendahl and Grasso, 1999, 2000; Bradford et al., 2011, 2013; Torkzaban et al., 2007]. Pore-scale visualization studies performed by Kuznar and Elimelech [2007] revealed that the particles attached in the secondary minimum translate along the collector surface due to hydrodynamic forces and get trapped in the rear stagnation point of the spherical collector grain where the hydrodynamic force is nil. Bergendahl and Grasso [2000] performed column experiments to show that the particles attached in the primary minimum can be detached via hydrodynamic shear by increasing the flow velocity. Johnson et al. [2007a] used torque balance calculations to show that the colloids deposited in the primary and secondary minima are vulnerable to hydrodynamic drag and can get detached. Lifting, sliding, and rolling are the hydrodynamic processes responsible for colloid detachment from the grain surface [Bergendahl and Grasso, 2000]. Rolling is often the dominant hydrodynamic mechanism for colloid detachment from the grain surface under laminar flow conditions [Bergendahl and Grasso, 2000; Bradford et al., 2011]. Hence, the fraction of mobile (or immobile) nanoparticles in the potential region can be found by performing a balance of hydrodynamic (T_H) and adhesive (T_A) torques for the particles in the potential region [Bergendahl and Grasso, 2000; Bradford et al., 2011, 2013; Johnson et al., 2007a; Torkzaban et al., 2007]. We followed the approach of Bradford et al. [2013] for performing the torque balance calculations, as briefly described below.

Figure 4 shows the forces and torques acting on a deformed particle adjacent to a smooth and chemically homogeneous surface. In this figure, a_0 is the radius of the nanoparticle-surface contact area due to particle deformation, which arises from adhesive force, $F_A = \frac{\partial \Phi}{\partial h}$, and is found as $a_0 = \left(\frac{4F_A a}{K}\right)^{1/3}$ using JKR theory [Bradford et al., 2011, 2013; Johnson et al., 1971, 2007a]. Here $K = \frac{4}{3\pi} \left[\frac{1-\nu_{nanoparticle}^2}{\pi E_{nanoparticle}} + \frac{1-\nu_{wall}^2}{\pi E_{wall}} \right]^{-1}$ is the composite Young's modulus [Johnson et al., 1971, 2007a], ν is the Poisson ratio, and E is the Young's modulus. The adhesive torque acting on the particle is $T_A = F_A a_0$ [Bradford et al., 2011, 2013; Torkzaban et al., 2007]. The

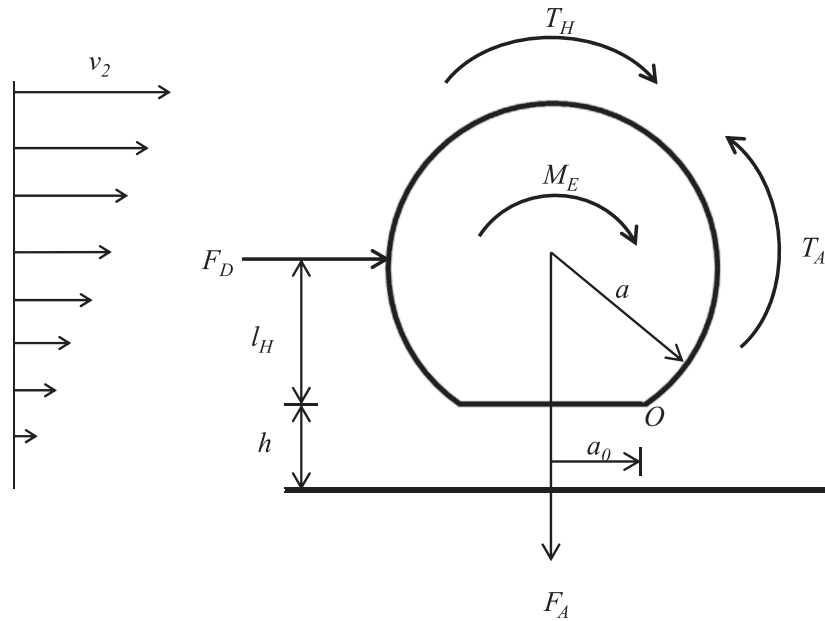


Figure 4. Forces and torques acting on a particle near to the collector surface (inspired from Bradford et al. [2013, Figure 1]).

fluid flow creates a drag force, F_D , acting on the nanoparticles, which is calculated as [Bradford et al., 2013; Duffadar and Davis, 2008; Goldman et al., 1967; O' Neill, 1968]

$$F_D = 6\pi\mu a \left(\frac{\partial v}{\partial h} \right) (h+a) F_D^* \tag{14}$$

where $F_D^* = \frac{1.7+1.022\frac{h}{a}}{1+1.046\frac{h}{a}-0.0015\left(\frac{h}{a}\right)^2}$ is a dimensionless function that accounts for the wall effects [Bradford et al., 2013; Duffadar and Davis, 2008]. The fluid velocity also creates a moment about the center of the particle, given as [Goldman et al., 1967]

$$M_E = 4\pi\mu a^3 \left(\frac{\partial v}{\partial h} \right) M_E^* \tag{15}$$

where $M_E^* = 0.055[18.277 - e^{-1.423\frac{h}{a}}]$ is a dimensionless function [Bradford et al., 2013; Duffadar and Davis, 2008]. The hydrodynamic torque acting on the particle at a distance of h from the wall is $T_H = F_D l_H + M_E$ [Bradford et al., 2013], where $l_H = \sqrt{a^2 - a_0^2}$ is the lever arm. Nanoparticles are mobile in the region where $T_H > T_A$ and nanoparticles are immobile in the region where $T_H \leq T_A$ [Bergendahl and Grasso, 2000; Bradford et al., 2011, 2013; Johnson et al., 2007a; Torkzaban et al., 2007]. The fraction of mobile particles accumulated in the secondary minimum region of a Type-I energy profile is then calculated as

$$f_2' = \int_{\delta s'}^{\delta s} e^{-\Phi/k_B T} dh / \int_{\delta s}^{\delta s} e^{-\Phi/k_B T} dh \tag{16}$$

where $\delta s'$ is the distance from the collector surface beyond which particles are mobile in the secondary minimum region, found from the torque balance calculations. For the range of values of parameters considered in this study, torque balance calculations revealed that the particles in the primary minimum region of a Type-I energy profile are immobile. The expressions for k_{ds} , k_{sd} , and f_2' for a Type-II energy profile are same as that given in equations (13) and (16).

Following the same approach described above, the expressions for k_{dp} , k_{pd} , and f'_1 for a Type-III energy profile are derived and are given in equation (17).

$$k_{dp} = \frac{D|_{\delta_\phi}}{K_B T} \frac{d\Phi}{dh} \Big|_{\delta_\phi}, \quad k_{pd} = \frac{D|_{\delta_\phi}}{\int_{\delta_p}^{\delta_\phi} e^{-\Phi/k_B T} dh} \frac{d\Phi}{dh} \Big|_{\delta_\phi} \frac{e^{-\Phi/k_B T}|_{\delta_\phi}}{k_B T}, \quad f'_1 = \int_{\delta_p'}^{\delta_\phi} e^{-\Phi/k_B T} dh / \int_{\delta_p}^{\delta_\phi} e^{-\Phi/k_B T} dh \quad (17)$$

where δ_p' is the distance from the grain surface beyond which particles are mobile in the potential region, found from the torque balance calculations.

2.3. Interaction Energy Calculation

The total interaction energy between the nanoparticle and the collector is calculated using DLVO theory and is expressed as the sum of electrostatic double layer repulsive energy, London-van der Waals interaction energy and Born potential energy by treating the particle-collector system as a sphere-plate interaction [Loveland et al., 1996; Wood et al., 2004]. The total dimensionless interaction energy, Φ^* , is given as

$$\Phi^* = \frac{\Phi}{k_B T} = \frac{\Phi_{EDL}}{k_B T} + \frac{\Phi_{VDW}}{k_B T} + \frac{\Phi_{Born}}{k_B T} \quad (18)$$

where Φ_{EDL} is the electric double layer energy, Φ_{VDW} is the London-van der Waals energy, and Φ_{Born} is the Born potential energy.

The electrostatic double layer energy is calculated by assuming constant surface potentials on nanoparticle and collector using the dimensionless form of Hogg-Healy-Fuerstenau (HHF) expression [Hogg et al., 1966] given by Rajagopalan and Kim [1981]. The expression is given in section A3, which contains three dimensionless parameters, N_{E1} , N_{E2} , and N_{DL} , given as

$$N_{E1} = \frac{\pi \epsilon \epsilon_0 a (\psi_1^2 + \psi_2^2)}{k_B T}; \quad N_{E2} = \frac{2(\psi_1/\psi_2)}{1 + (\psi_1/\psi_2)^2}; \quad N_{DL} = \kappa a \quad (19)$$

Here ψ_1 and ψ_2 are the surface potentials on the nanoparticle and collector, respectively, ϵ is the dielectric constant of water, ϵ_0 is the permittivity of vacuum, $\kappa = \sqrt{2000 N_A l e^2 / \epsilon \epsilon_0 k_B T}$ is the inverse Debye-Huckel length, N_A is Avogadro number, l is the solution ionic strength, and e is the elementary charge. N_{E1} , N_{E2} , and N_{DL} are the dimensionless parameters representing the magnitudes of surface potentials, the ratio of surface potentials, and the ratio of particle radius to double layer thickness, respectively [Rajagopalan and Kim, 1981]. HHF formula is valid for 1:1 electrolytes when $N_{DL} > 5$ and ψ_1 and $\psi_2 < 60$ mV. London-van der Waals interaction energy is calculated using the expression derived by Gregory [1981] for retarded sphere-plate interaction for $h^* \leq 0.2$ and Czarnecki's expression [Gregory, 1981] for $h^* > 0.2$. The expressions for London-van der Waals interaction energy are given in section A3, and they contain two parameters, namely, $\lambda^* = \lambda/a$ and H , where λ is the characteristic wavelength of the interaction, usually taken as 100 nm, and H is the Hamaker constant. Born potential energy is calculated using the expression given by Ruckenstein and Prieve [1976] (section A3) which contains a parameter $\sigma^* = \sigma/a$, where σ is the collision diameter, usually assumed as 0.5 nm.

2.4. Nondimensionalization of the Governing Equations

The governing equations are nondimensionalized using the following dimensionless variables

$$c^* = \frac{c}{c_0}; \quad r^* = \frac{r}{R}; \quad z^* = \frac{z}{R}; \quad t^* = \frac{t v_m}{R}; \quad \bar{s}_1^* = \frac{\bar{s}_1}{c_0 R}; \quad \bar{s}_2^* = \frac{\bar{s}_2}{c_0 R} \quad (20)$$

where c_0 is the nanoparticle concentration at $z=0$. The following dimensionless parameters are also used in the dimensional analysis

$$Pe = \frac{v_m R}{D_\infty}; \quad A = \frac{a}{R}; \quad Da_{ds} = \frac{k_{ds}}{v_m}; \quad Da_{sd} = \frac{k_{sd} R}{v_m}; \quad Da_{sp} = \frac{k_{sp} R}{v_m}; \quad Da_{ps} = \frac{k_{ps} R}{v_m}; \quad Da_{dp} = \frac{k_{dp}}{v_m}; \quad Da_{pd} = \frac{k_{pd} R}{v_m} \quad (21)$$

where Pe is the Péclet number (ratio of the rate of advective transport to the rate of diffusive transport), A is the interception parameter (ratio of nanoparticle radius to pore radius), Da_{ds} , Da_{sd} , Da_{sp} , Da_{ps} , Da_{dp} , and

Da_{pd} are the various Damköhler numbers (ratio of adsorption rate to the rate of advective transport) corresponding to k_{ds} , k_{sd} , k_{sp} , k_{ps} , k_{dp} , and k_{pd} , respectively. The governing equations (2), (3), (5), (7), and (8) can be rewritten in terms of the dimensionless variables and parameters as follows

$$\frac{\partial c^*}{\partial t^*} = \frac{1}{Pe} \frac{1}{r^*} \frac{\partial}{\partial r^*} \left(r^* \frac{\partial c^*}{\partial r^*} \right) + \frac{1}{Pe} \frac{\partial^2 c^*}{\partial z^{*2}} - 2[1-r^{*2}] \frac{\partial c^*}{\partial z^*}; \quad 0 \leq r^* \leq 1 - \delta_D^* \quad (22)$$

$$\frac{\partial c^*}{\partial t^*} = \frac{1}{Pe} \frac{1}{r^*} \frac{\partial}{\partial r^*} \left(r^* f_1(r^*) \frac{\partial c^*}{\partial r^*} \right) + \frac{1}{Pe} \frac{\partial}{\partial z^*} \left(f_4(r^*) \frac{\partial c^*}{\partial z^*} \right) - 2[1-r^{*2}] \frac{\partial c^*}{\partial z^*}; \quad 1 - \delta_D^* \leq r^* \leq 1 - \delta_\phi^* \quad (23)$$

$$\frac{\partial \bar{s}_2^*}{\partial t^*} = -\bar{v}_2^* f_2' \frac{\partial \bar{s}_2^*}{\partial z^*} + Da_{ds} c^* \Big|_{1-\delta_\phi^*} - Da_{sd} \bar{s}_2^* - Da_{sp} \bar{s}_2^* + Da_{ps} \bar{s}_1^* \quad (24a)$$

$$\frac{\partial \bar{s}_1^*}{\partial t^*} = Da_{sp} \bar{s}_2^* - Da_{ps} \bar{s}_1^* \quad (24b)$$

$$\frac{\partial \bar{s}_2^*}{\partial t^*} = -\bar{v}_2^* f_2' \frac{\partial \bar{s}_2^*}{\partial z^*} + Da_{ds} c^* \Big|_{1-\delta_\phi^*} - Da_{sd} \bar{s}_2^* \quad (25)$$

$$\frac{\partial \bar{s}_1^*}{\partial t} = -\bar{v}_1^* f_1' \frac{\partial \bar{s}_1^*}{\partial z^*} + Da_{dp} c^* \Big|_{1-\delta_\phi^*} - Da_{pd} \bar{s}_1^* \quad (26)$$

2.5. Solution of the Governing Equations

Equations (22)–(26) constitute the complete set of coupled equations governing the transport of nanoparticles in a cylindrical pore, with equations (24)–(26) describing, respectively, the nanoparticle deposition for Type-I, Type-II, and Type-III energy profiles. The governing equations are solved subject to the following initial and boundary conditions

$$c^*(r^*, z^*, 0) = 0; \quad \bar{s}_1^*(z^*, 0) = \bar{s}_2^*(z^*, 0) = 0 \quad (27)$$

$$c^*(r^*, 0, t^*) = \begin{cases} 1, & t^* \leq t_m^* \\ 0, & t^* > t_m^* \end{cases}; \quad \bar{s}_1^*(0, t^*) = \bar{s}_2^*(0, t^*) = 0 \quad (28)$$

$$\frac{\partial c^*}{\partial z^*}(r^*, L^*, t^*) = 0 \quad (29)$$

$$\frac{\partial c^*}{\partial r^*}(0, z^*, t^*) = 0 \quad (30)$$

where t_m^* is the duration of the input pulse (dimensionless) and L^* is the dimensionless length of the pore. Equation (27) indicates that there is no particle present inside the pore initially. Equations (28) and (29) represent the Dirichlet and Neumann boundary conditions at the inlet and the outlet of the pore, respectively. Equation (30) represents the zero flux condition across the tube center due to axial symmetry.

At the diffusion region-potential region interface, flux continuity is ensured by imposing the following interface condition

$$-\frac{f_1(r^*)}{Pe} \frac{\partial c^*}{\partial r^*} \Big|_{1-\delta_\phi^*} = -Da_{ds} c^* \Big|_{1-\delta_\phi^*} + Da_{sd} \bar{s}_2^* \quad \text{for Type-I and Type-II energy profiles} \quad (31a)$$

$$-\frac{f_1(r^*)}{Pe} \frac{\partial c^*}{\partial r^*} \Big|_{1-\delta_\phi^*} = -Da_{dp} c^* \Big|_{1-\delta_\phi^*} + Da_{pd} \bar{s}_1^* \quad \text{for a Type-III energy profile} \quad (31b)$$

Governing equations (22)–(26) subject to the initial and boundary conditions (27)–(31) are solved numerically using COMSOL Multiphysics software which uses Galerkin Finite Element Method.

The nanoparticle concentration obtained from the pore-scale model is averaged over a moving averaging volume within the pore to obtain the 1-D nanoparticle concentration field (as a function of distance). The nanoparticle breakthrough concentration, \bar{c}^* , is obtained by averaging the concentration of mobile nanoparticles

Table 1. Pore-Scale Parameters

Parameter	Definition	Interpretation
N_{E1}	$\frac{\pi\epsilon\epsilon_0 a (\psi_1^2 + \psi_2^2)}{k_B T}$	Represents the magnitudes of surface potentials
N_{E2}	$\frac{2(\psi_1/\psi_2)}{1+(\psi_1/\psi_2)^2}$	Ratio of surface potentials
N_{DL}	$\frac{r}{ka}$	Ratio of nanoparticle radius to double layer thickness
Pe	$\frac{v_m R}{D_\infty}$	Péclet number
A	$\frac{a}{R}$	Interception parameter
λ^*	λ/a	Ratio of characteristic wavelength of interaction to the nanoparticle radius

over the averaging volume. Similarly, the average attached concentration, \bar{s}^* , is obtained by averaging the concentration of immobile nanoparticles over the surface of the pore within the moving averaging volume.

2.6. Pore-Scale Parameters Governing Nanoparticle Transport

The six dimensionless pore-scale parameters involved in the model are N_{E1} , N_{E2} , N_{DL} , Pe , A , and λ^* . The definitions and the physical interpretation of these dimensionless parameters are given in Table 1.

2.7. Model Verification

In order to verify our formulation of nanoparticle transport in the potential region (i.e., equations (24)–(26)) and interface conditions (equation (31)), the solution of equations (22)–(26) is compared with the model of Seetha et al. [2014], who solved the full transport equation for virus-sized colloids in a cylindrical pore. In particular, we compared averaged breakthrough curves and attached concentration curves obtained from the two models. For the model verification, all particles in the potential region are assumed to be immobile ($f'_1=f'_2=0$). The parameter values are chosen to be $\lambda^*=2$, $A=0.001$, $N_{E2}=1$, $N_{DL}=25$, $Pe=5$, and (a) $N_{E1}=10$ for a Type-I energy profile or (b) $N_{E1}=40$ for a Type-II energy profile. The values of the other model parameters which remain constant for all simulations are given in Table 2. Figure 5 compares the nanoparticle breakthrough curve and the average attached concentration curve obtained from our model with that of Seetha et al. [2014]. The good agreement between the two models verifies the accuracy of the expressions for the average mass transfer rate coefficients (equations (10), (13), and (16)) used in this work.

3. Modeling Average (1-D) Nanoparticle Transport in a Single Pore

The nanoparticle transport at 1-D pore scale is described using advection-dispersion-adsorption equation. The nanoparticle attachment is modeled either as equilibrium adsorption (equation (32)) or as kinetic adsorption (equation (33)).

$$R_f \frac{\partial \bar{c}^*}{\partial t^*} = \frac{1}{Pe_{(1D)}} \frac{\partial^2 \bar{c}^*}{\partial z^{*2}} - \bar{v}^* \frac{\partial \bar{c}^*}{\partial z^*} \tag{32a}$$

$$\bar{s}^* = K_D \bar{c}^* \tag{32b}$$

$$\frac{\partial \bar{c}^*}{\partial t^*} = \frac{1}{Pe_{(1D)}} \frac{\partial^2 \bar{c}^*}{\partial z^{*2}} - \bar{v}^* \frac{\partial \bar{c}^*}{\partial z^*} - Da_{att} \bar{c}^* + 2Da_{det} \bar{s}^* \tag{33a}$$

$$\frac{\partial \bar{s}^*}{\partial t^*} = \frac{Da_{att}}{2} \bar{c}^* - Da_{det} \bar{s}^* \tag{33b}$$

Table 2. Other Model Parameters Used in the Simulations

Dimensional Parameter	Value
Permittivity of vacuum, ϵ_0	$8.85419 \times 10^{-12} \text{ C}^2/\text{J}\cdot\text{m}$
Collision diameter, σ	0.5 nm
Characteristic wavelength, λ	100 nm
Boltzmann constant, k_B	$1.38 \times 10^{-23} \text{ J/K}$
Avogadro number, N_A	6.023×10^{23}
Electron charge, e	$1.6 \times 10^{-19} \text{ C}$
Poisson ratio of nanoparticle, ν_1	0.3
Poisson ratio of collector, ν_2	0.2
Young's modulus of nanoparticle, E_1	1 GPa
Young's modulus of collector, E_2	50 GPa

where $R_f=1+2K'_D$ is the retardation factor, $K'_D=K_D/R$ is the dimensionless equilibrium distribution coefficient, K_D [L] is the equilibrium distribution coefficient, $Pe_{(1D)}=v_m R/D_L=Pe/[1+\frac{1}{48}Pe^2(1-2\delta_\phi^*)^2]$ is the 1-D Péclet number, D_L is the pore-scale dispersion coefficient calculated using the expression derived by James and Chrysikopoulos [2003] as $D_L=D_\infty[1+\frac{1}{48}Pe^2(1-2\delta_\phi^*)^2]$, \bar{v}^* is the average velocity of mobile particles, $Da_{att}=k_{att}R/v_m$ is the Damköhler number corresponding to the

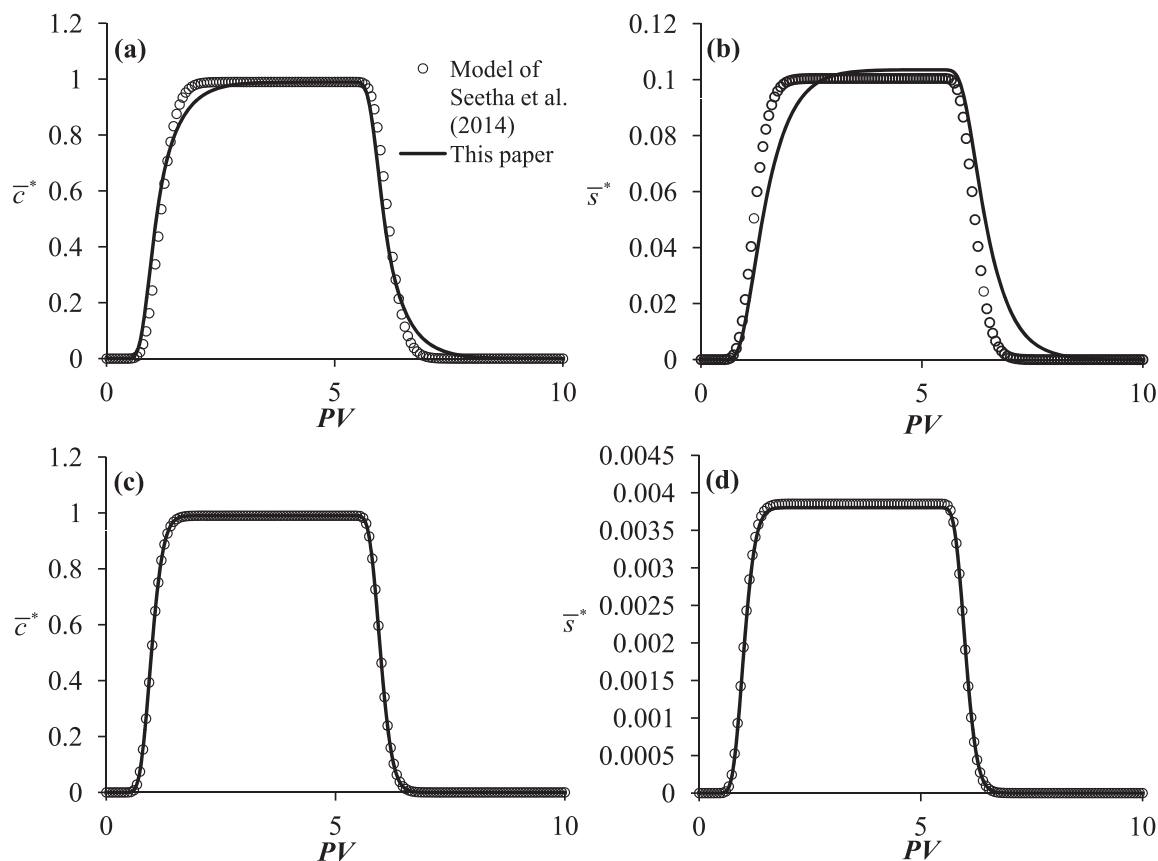


Figure 5. Comparison of the (left column) nanoparticle BTCs and (right column) attached concentration curves obtained from model developed in this study (solid lines) with that of Seetha *et al.* [2014] (hollow circles) for (a and b) Type-I and (c and d) Type-II energy profiles.

rate coefficient for nanoparticle attachment to the pore wall, $Da_{det} = k_{det}R/v_m$ is the Damköhler number corresponding to the rate coefficient for nanoparticle detachment from the pore wall, and k_{att} [T^{-1}] and k_{det} [T^{-1}] are the average rate coefficients for nanoparticle attachment and detachment at pore scale.

The values of the average nanoparticle deposition coefficients at pore scale (K'_D in the case of an equilibrium model, and Da_{att} and Da_{det} in the case of a kinetic model) are estimated by fitting the nanoparticle BTC (or the average attached concentration curve) obtained from the pore-scale model (section 2) against 1-D advection-dispersion-adsorption model (equation (32) or (33)). These equations are solved numerically using an alternating three-step operator splitting approach [Barry *et al.*, 2000; Gasda *et al.*, 2011; Kaluarachchi and Morshed, 1995; Seetha *et al.*, 2015]. This method is based on splitting the coupled set of governing equations into advection, dispersion, and reaction operators which are then solved sequentially over the first half of each time step with the order of the solution of the advection, dispersion, and reaction operators switched in the second half of each time step [Seetha *et al.*, 2015]. An explicit finite volume method based on Monotone Upwind Schemes for Conservation Laws is used to solve advective part which is globally second-order accurate and non-oscillatory [Putti *et al.*, 1990; Ratha *et al.*, 2009; Soraganvi and Mohan Kumar, 2009]. We use a second-order Godunov-type scheme with a minmod limiter for the piecewise linear interpolation of concentration in each cell for calculating the advective flux at the cell interfaces, and Hancock's scheme for time splitting which is a two-step second-order accurate explicit scheme [Putti *et al.*, 1990; Ratha *et al.*, 2009; Soraganvi and Mohan Kumar, 2009]. The stability of the above scheme depends on Courant number, $c_u = \frac{v\Delta t}{\Delta z}$, which should be less than 1. The dispersive part is solved using a fully implicit finite difference method, and the reaction part using a fourth-order Runge-Kutta method. The conditions for nanoparticle deposition are said to be favorable when the average attachment rate coefficient is greater than the average detachment rate coefficient and unfavorable vice versa.

Figure 6 shows the nanoparticle BTC and the attached concentration curve obtained from the pore-scale model for a cylindrical pore and the corresponding fitted curves from the 1-D model with kinetic adsorption

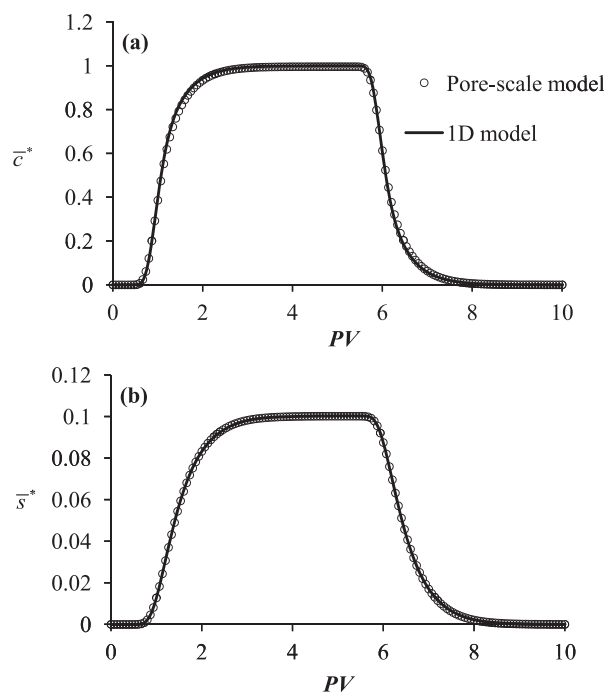


Figure 6. Comparison of (a) nanoparticle BTC and (b) attached concentration curve obtained from the pore-scale model (circles) and the 1-D pore-scale model (solid line) for $\lambda^* = 2$, $A = 0.001$, $Pe = 5$, $N_{E1} = 10$, $N_{E2} = 1$, and $N_{DL} = 25$.

that for nanoparticles, the collision efficiency is least affected by the parameter N_{E2} . The effect of various pore-scale parameters on the colloid concentration at steady state and the favorability of the surface for adsorption have been previously explained by *Seetha et al.* [2014]. In this paper, applying transient simulations, we explore how various pore-scale parameters affect the deposition rate coefficients.

As N_{E1} increases, the electrostatic repulsion between the nanoparticle and the grain surface increases. This reduces the primary and secondary minimum depth and increases the height of the energy barrier making the conditions less favorable for particle deposition. As a result, K'_D decreases with increasing N_{E1} (Figure 7a). The diffuse double layers around the particle and collector get compressed with increasing N_{DL} , leading to a reduction in the repulsive double layer forces, which in turn increases the depth of primary and secondary minima and decreases the height of the energy barrier. Hence, the favorability of the surface for adsorption increases with increasing N_{DL} and as a result, K'_D increases (Figure 7b). As Pe increases, advection dominance increases, reducing the rate of particle transfer to the potential region by transverse diffusion. Hence, K'_D decreases with increasing Pe (Figure 7c). Furthermore, K'_D increases with increasing A (Figure 7d) and λ^* (Figure 7e). The reasons behind these observed trends are explained using the dimensional expressions for the deposition rate coefficients in the following paragraphs.

5. Correlation Equations for Deposition Rate Coefficients at Pore Scale

Pore-scale simulations for nanoparticle transport are performed for a range of values of pore-scale parameters selected from the literature (Table 3). The favorability of the surface for deposition is dictated by the magnitudes of peaks in the DLVO energy profile (which is a function of N_{E1} , N_{E2} , N_{DL} , and λ^*), Pe and A [*Seetha et al.*, 2014]. In order to cover an adequate range of DLVO energy profiles describing the favorable and unfavorable conditions, the pore-scale simulations are performed for various combinations of the pore-scale parameter values, which resulted in a total of 1350 pore-scale simulations. In all simulations, the input nanoparticle pulse is applied for five pore volumes (PVs), followed by particle-free solution for another five PVs.

The estimated values of the average nanoparticle deposition parameters (K'_D or Da_{att} and Da_{det}) obtained from above mentioned pore-scale simulations formed the data set that was used to develop correlation

(equation (33)). It can be seen that the 1-D model accurately fits the BTC and the attached concentration curve.

4. Average Deposition Rate Coefficients Versus Pore-Scale Parameters

Figure 7 shows the effect of various pore-scale parameters on the equilibrium adsorption rate coefficient at pore scale. Unless otherwise specified, the parameter values used in the simulations are $\lambda^* = 5$, $Pe = 0.05$, $A = 0.001$, $N_{E1} = 40$, $N_{E2} = 1$, and $N_{DL} = 50$. For these set of parameter values, an equilibrium model best describes nanoparticle deposition onto the pore surface. N_{E2} is found to have negligible effect on the average deposition rate coefficients, for the range of parameter values considered in this study. Hence, its variation is not considered in the development of the correlation equations (section 5). This is also supported by the triangular network simulation results of *Chang and Chan* [2008] for colloid transport, who found

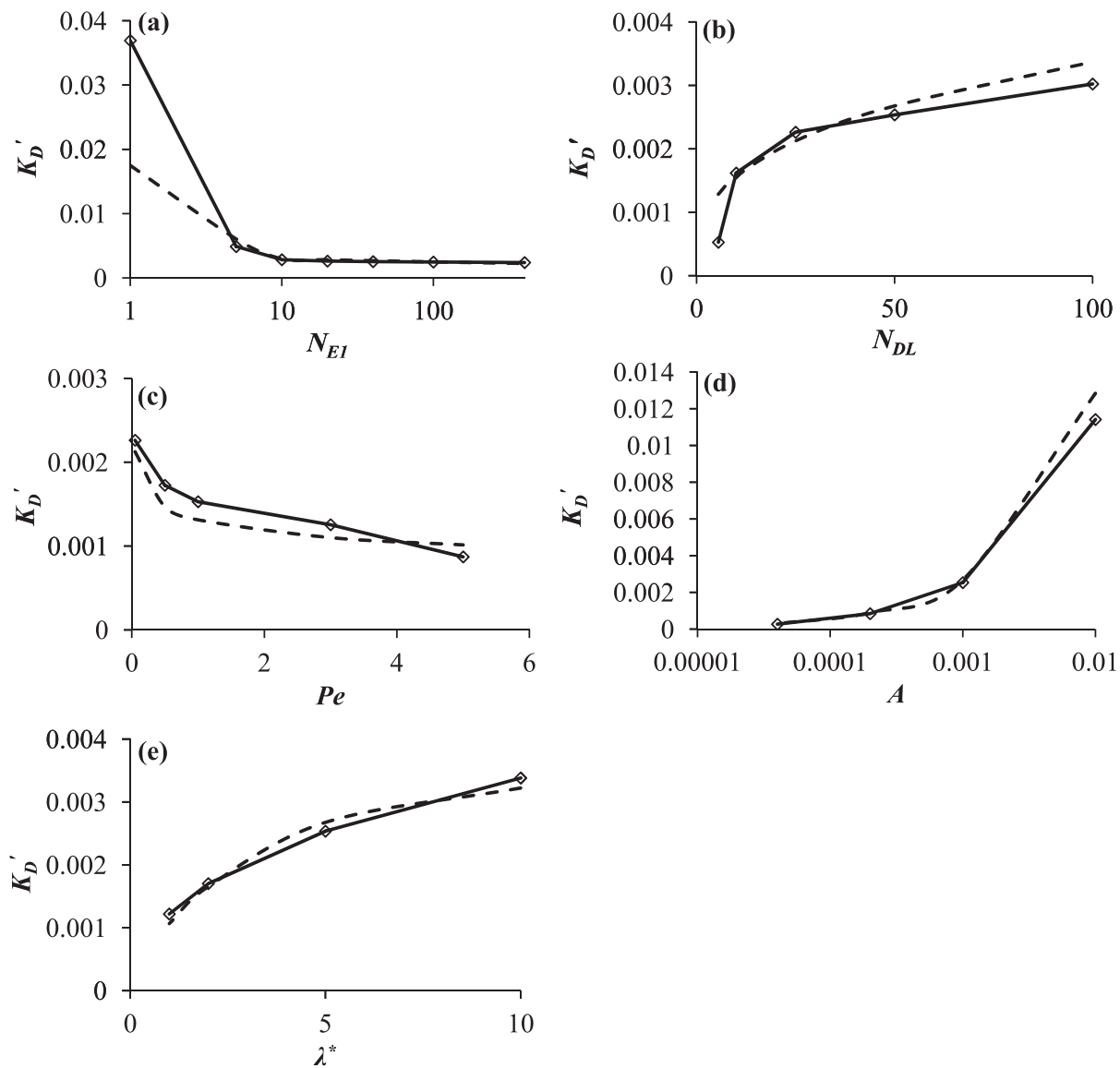


Figure 7. Effect of various pore-scale parameters, (a) N_{E1} , (b) N_{DL} , (c) Pe , (d) A , and (e) λ^* , on equilibrium adsorption coefficient (solid line: fitted values from the 1-D pore-scale model, dotted line: predicted values from the correlation equation).

equations (equations (34) and (35)) for the pore-averaged deposition rate coefficients (K'_D or Da_{att} and Da_{det}) in terms of the five pore-scale parameters (N_{E1} , N_{DL} , Pe , A , and λ^*).

$$K'_D = p_1 N_{E1}^{p_2} N_{DL}^{p_3} Pe^{p_4} A^{p_5} \lambda^{*p_6} \quad (34)$$

$$Da_{(att)} = q_1 N_{E1}^{q_2} N_{DL}^{q_3} Pe^{q_4} A^{q_5} \lambda^{*q_6} \quad (35a)$$

$$Da_{(det)} = r_1 N_{E1}^{r_2} N_{DL}^{r_3} Pe^{r_4} \exp(r_5 A) \lambda^{*r_6} \quad (35b)$$

In equations (34) and (35), p_i , q_i , and r_i ($i = 1, 2, \dots, 6$) are the coefficients in the correlation equations for K'_D , Da_{att} , and Da_{det} , respectively. The values of these coefficients are estimated by regressing the logarithm of the dimensionless pore-scale parameters against the logarithm of the estimated nanoparticle deposition parameters.

Table 3. Range of Parameter Values Used in the Simulations^a

Parameter	Value
N_{E1}	1–400
N_{E2}	0.8–1
N_{DL}	5.5–100
Pe	0.05–50
A	0.00004–0.01
λ^*	1–10

^aThe sources for these values are referred in Seetha et al. [2014].

Table 4. Values of Coefficients in the Correlation Equations for the Deposition Rate Coefficients of Group I Nanoparticles

Favorability	Unfavorable ($N_{E1} < 10$)									Unfavorable ($N_{E1} \geq 10$)																				
	≤ 5			>5			≤ 5			>5																				
Pe	≤ 0.01			≤ 0.001			>0.001			≤ 0.01			≤ 0.001			>0.001														
Coefficients of dimensionless expression ^a	p_1	1.103	q_1	0.099	r_1	0.873	q_1	1.161×10^{-5}	r_1	0.873	p_1	0.043	q_1	7.927×10^{-3}	r_1	4.896	q_1	1.193×10^{-7}	r_1	4.896										
	p_2	-0.659	q_2	-0.762	r_2	0.426	q_2	-0.748	r_2	0.426	p_2	-0.078	q_2	-0.109	r_2	0.026	q_2	-0.162	r_2	0.026										
	p_3	0.443	q_3	0.561	r_3	-0.207	q_3	0.737	r_3	-0.207	p_3	0.333	q_3	0.442	r_3	-0.149	q_3	0.679	r_3	-0.149										
	p_4	-0.137	q_4	-1.176	r_4	-0.812	q_4	-0.981	r_4	-0.812	p_4	-0.161	q_4	-1.221	r_4	-0.737	q_4	-1.043	r_4	-0.737										
	p_5	0.686	q_5	0.134	r_5	-480	q_5	-0.916	r_5	-480	p_5	0.681	q_5	0.206	r_5	-412	q_5	-1.039	r_5	-412										
	p_6	-0.963	q_6	-0.725	r_6	1.128	q_6	-0.505	r_6	1.128	p_6	0.268	q_6	0.523	r_6	0.355	q_6	1.078	r_6	0.355										
%RMSE	8.8			10.2			58.3			10.2			58.3			3.08			4.8			61.5			3.5			61.5		
R^2	0.85			0.83			0.86			0.92			0.86			0.98			0.94			0.88			0.99			0.88		
Coefficients of dimensional expression ^b	m_2	0.88	n_2	1.042	o_2	0.529	n_2	1.117	o_2	0.529	m_2	0.244	n_2	0.33	o_2	0.100	n_2	0.502	o_2	0.101										
	m_3	0.574	n_3	1.657	o_3	0.489	n_3	1.36	o_3	0.489	m_3	0.072	n_3	1.109	o_3	0.786	n_3	0.865	o_3	0.786										
	m_4	0.137	n_4	1.176	o_4	0.812	n_4	0.981	o_4	0.812	m_4	0.161	n_4	1.221	o_4	0.737	n_4	1.043	o_4	0.737										
	m_5	0.658	n_5	0.762	o_5	0.426	n_5	0.748	o_5	0.426	m_5	0.077	n_5	0.109	o_5	0.026	n_5	0.162	o_5	0.026										
	m_6	0.221	n_6	0.280	o_6	0.103	n_6	0.369	o_6	0.103	m_6	0.166	n_6	0.221	o_6	0.075	n_6	0.340	o_6	0.075										
	m_7	0.137	n_7	0.176	o_7	0.188	n_7	-0.019	o_7	0.188	m_7	0.161	n_7	0.221	o_7	0.263	n_7	0.043	o_7	0.263										
	m_8	0.177	n_8	2.31	o_8	1.812	n_8	1.065	o_8	1.812	m_8	0.158	n_8	2.427	o_8	1.737	n_8	1.004	o_8	1.737										
	m_9	1.296	n_9	0.518	o_9	1.721	n_9	1.403	o_9	1.721	m_9	0.507	n_9	1.205	o_9	1.216	n_9	2.642	o_9	1.216										
				o_{10}	480			o_{10}	480				o_{10}	412			o_{10}	412			o_{10}	412			o_{10}	412				

^aCoefficients in equations (34) and (35).

^bCoefficients in equations (36) and (37).

Based on the nanoparticle size, the data are classified into three groups: Group I ($\lambda^* \geq 5$), Group II ($2 \leq \lambda^* < 5$), and Group III ($1 \leq \lambda^* < 2$). Correlation equations for each group could be found only under unfavorable conditions for deposition. In this study, pore-scale simulations are performed for three values of Péclet number, $Pe = 0.05, 5, \text{ and } 50$. Under unfavorable conditions, nanoparticle deposition onto the pore wall is best described by (a) an equilibrium model at low Péclet numbers ($Pe = 0.05$) and (b) a kinetic model at high Péclet numbers ($Pe = 50$). But, there seems to be an intermediate range (around $Pe = 5$), where both equilibrium and kinetic models fit the 1-D concentration field.

The estimated values of coefficients in equations (34) and (35) for the three nanoparticle groups are given in Tables 4–6. Figure 7 compares the estimated deposition rate coefficients from the pore-scale model with that predicted by the correlation expressions (equations (34) and (35)). It can be seen that there is a reasonable agreement between the calculated values and those calculated by the correlation equation. Equations (34) and (35) can be written in dimensional form, which results in correlation equations for K_D , k_{att} , and k_{det} in terms of nine dimensional pore-scale parameters ($\varepsilon, T, \mu, \psi_1, \psi_2, l, v_m, R$, and a) as

$$K_D = m_1 \varepsilon^{-m_2} T^{m_3} \mu^{-m_4} (\psi_1^2 + \psi_2^2)^{-m_5} l^{m_6} v_m^{-m_7} R^{m_8} a^{m_9} \quad (36)$$

$$k_{att} = n_1 \varepsilon^{-n_2} T^{n_3} \mu^{-n_4} (\psi_1^2 + \psi_2^2)^{-n_5} l^{n_6} v_m^{-n_7} R^{-n_8} a^{-n_9} \quad (37a)$$

$$k_{det} = o_1 \varepsilon^{o_2} T^{o_3} \mu^{-o_4} (\psi_1^2 + \psi_2^2)^{o_5} l^{-o_6} v_m^{o_7} R^{-o_8} a^{-o_9} \exp(-o_{10}(a/R)) \quad (37b)$$

In equations (36) and (37), m_i, n_i , and o_j ($i = 1, 2, \dots, 9; j = 1, 2, \dots, 10$) are constants, whose values are given in Tables 4–6. Values of coefficients m_1, n_1 , and o_1 depend on $N_A, k_B, e, \varepsilon_0$, and λ , as given below

$$m_1 = p_1 \pi^{p_2 + p_4} 2000^{p_3} / 2 \cdot 6^{p_4} \left[N_A^{0.5p_3} k_B^{-(p_2 + 0.5p_3 + p_4)} e^{p_3} \varepsilon_0^{p_2 - 0.5p_3} \lambda^{p_6} \right] \quad (38)$$

$$n_1 = q_1 \pi^{q_2 + q_4} 2000^{q_3} / 2 \cdot 6^{q_4} \left[N_A^{0.5q_3} k_B^{-(q_2 + 0.5q_3 + q_4)} e^{q_3} \varepsilon_0^{q_2 - 0.5q_3} \lambda^{q_6} \right] \quad (39)$$

$$o_1 = r_1 \pi^{r_2 + r_4} 2000^{r_3} / 2 \cdot 6^{r_4} \left[N_A^{0.5r_3} k_B^{-(r_2 + 0.5r_3 + r_4)} e^{r_3} \varepsilon_0^{r_2 - 0.5r_3} \lambda^{r_6} \right] \quad (40)$$

In deriving the correlation equations, we have assumed that the collector surface is smooth and chemically homogeneous. The correlation equations predict $k_{att} \ll k_{det}$ which is in contrast with some experimentally observed colloid retentions under unfavorable conditions. This implies that processes other than

Table 5. Values of Coefficients in the Correlation Equations for the Deposition Rate Coefficients of Group II Nanoparticles

Favorability		Unfavorable ($N_{E1} \geq 20$)										
Pe		≤ 5					> 5					
A		≤ 0.01		≤ 0.001			> 0.001					
Coefficients of dimensionless expression ^a	p_1	0.026	q_1	0.049	r_1	22.269	q_1	2.878×10^{-6}	r_1	22.269		
	p_2	-0.078	q_2	-0.113	r_2	0.006	q_2	-0.182	r_2	0.006		
	p_3	0.321	q_3	0.395	r_3	-0.116	q_3	0.701	r_3	-0.116		
	p_4	-0.165	q_4	-1.247	r_4	-0.816	q_4	-1.068	r_4	-0.816		
	p_5	0.655	q_5	0.299	r_5	-413	q_5	-1.034	r_5	-413		
	p_6	0.474	q_6	0.045	r_6	-0.489	q_6	-0.892	r_6	-0.489		
%RMSE		2.7		4.8		72		4		72		
R^2		0.98		0.94		0.92		0.98		0.92		
Coefficients of dimensional expression ^b	m_2	0.238	n_2	0.311	o_2	0.064	n_2	0.533	o_2	0.064		
	m_3	0.082	n_3	1.162	o_3	0.868	n_3	0.899	o_3	0.868		
	m_4	0.165	n_4	1.247	o_4	0.816	n_4	1.068	o_4	0.816		
	m_5	0.078	n_5	0.113	o_5	0.006	n_5	0.182	o_5	0.006		
	m_6	0.161	n_6	0.197	o_6	0.058	n_6	0.351	o_6	0.058		
	m_7	0.165	n_7	0.247	o_7	0.184	n_7	0.068	o_7	0.184		
	m_8	0.180	n_8	2.546	o_8	1.816	n_8	1.034	o_8	1.816		
	m_9	0.260	n_9	0.711	o_9	0.437	n_9	0.69	o_9	0.437		
					o_{10}	413			o_{10}	413		

^aCoefficients in equations (34) and (35).

^bCoefficients in equations (36) and (37).

nanoparticle-collector interactions, such as, physical and chemical heterogeneity of the nanoparticle and grain surface and the presence of stagnation points play a dominant role in nanoparticle deposition under unfavorable conditions. Though our model does not account for nanoparticle and grain surface roughness, the correlation equations show the contribution of various pore-scale parameters on nanoparticle deposition under unfavorable conditions.

6. Comparison With Experimental Data

In this section, first we explain in detail how deposition coefficients, K_D , k_{att} , and k_{det} , vary with the nine pore-scale parameters as predicted by the correlation equations (36) and (37). Then, whenever possible, we

Table 6. Values of Coefficients in the Correlation Equations for the Deposition Rate Coefficients of Group III Nanoparticles

Favorability		Unfavorable ($N_{E1} \geq 40$)										
Pe		≤ 5					> 5					
A		≤ 0.01		≤ 0.001			> 0.001					
Coefficients of dimensionless expression ^a	p_1	1.248×10^{-2}	q_1	4.387×10^{-2}	r_1	12.809	q_1	3.636×10^{-7}	r_1	12.809		
	p_2	-0.054	q_2	-0.084	r_2	0.008	q_2	-0.132	r_2	0.008		
	p_3	0.364	q_3	0.449	r_3	-0.034	q_3	0.725	r_3	-0.034		
	p_4	-0.179	q_4	-1.263	r_4	-0.905	q_4	-1.094	r_4	-0.905		
	p_5	0.611	q_5	0.384	r_5	-439	q_5	-1.069	r_5	-439		
	p_6	0.536	q_6	0.775	r_6	0.196	q_6	1.280	r_6	0.196		
%RMSE		2.83		3.34		58.34		3.25		58.34		
R^2		0.98		0.97		0.98		0.99		0.98		
Coefficients of dimensional expression ^b	m_2	0.236	n_2	0.308	o_2	0.025	n_2	0.495	o_2	0.025		
	m_3	0.051	n_3	1.122	o_3	0.914	n_3	0.864	o_3	0.914		
	m_4	0.179	n_4	1.263	o_4	0.905	n_4	1.094	o_4	0.905		
	m_5	0.054	n_5	0.084	o_5	0.008	n_5	0.132	o_5	0.008		
	m_6	0.182	n_6	0.224	o_6	0.017	n_6	0.363	o_6	0.017		
	m_7	0.179	n_7	0.263	o_7	0.095	n_7	0.094	o_7	0.095		
	m_8	0.210	n_8	2.646	o_8	1.905	n_8	1.025	o_8	1.905		
	m_9	0.205	n_9	1.289	o_9	1.126	n_9	2.851	o_9	1.126		
					o_{10}	439			o_{10}	439		

^aCoefficients in equations (34) and (35).

^bCoefficients in equations (36) and (37).

compare the predicted trends with the observed behaviors from the column-scale and pore-scale experiments.

When the dielectric constant of the solution increases, the electrostatic double layer repulsive force between the particle and the collector increases. Hence, nanoparticle deposition decreases, resulting in decreasing K_D and k_{att} and increasing k_{det} (equations (36) and (37) and Tables 4–6).

Equations (36) and (37) together with Tables 4–6 show that K_D and k_{att} increase, and k_{det} decreases with increasing temperature. As temperature increases, the solution viscosity decreases and, hence, the particle diffusion coefficient increases, thereby increasing the rate of particle transfer to the potential region. Also, with increasing temperature, the surface potentials of the particle and the surface, and the dielectric constant of the solution decrease [Adamczyk, 2006; Rodriguez and Araujo, 2006; Yan *et al.*, 2015], and the inverse Debye length decreases, thus reducing the electrostatic repulsive force between the particle and the collector. Thus, deeper minima, lesser energy barrier together with increased particle transfer to the wall region results in an increase in the particle deposition with increasing temperature. This finding is consistent with the experimental observations available in the literature [Chrysikopoulos and Aravantinou, 2014; Syngouna and Chrysikopoulos, 2010; Yan *et al.*, 2015]. Chrysikopoulos and Aravantinou [2014] found from batch experiments under static conditions that temperature significantly affects virus attachment, and the attachment increased with increasing temperature. They found that the Freundlich isotherm fitted the data and the Freundlich constant of MS2 and $\Phi X174$ onto quartz sand was greater at 20°C than at 4°C. Syngouna and Chrysikopoulos [2010] conducted batch experiments to study the effect of temperature on MS2 and $\Phi X174$ adsorption onto kaolinite and bentonite, and found that the equilibrium distribution coefficient increased when the temperature was increased from 4 to 25°C. Yan *et al.* [2015] conducted experiments in a microfluidic system to investigate the thermal effect on kinetics of colloid deposition onto the solid surface. They observed that the dimensionless colloid deposition rate (Sherwood number) increased by 265% when the solution temperature was increased from 20 to 70°C.

When fluid viscosity increases, the nanoparticle diffusion coefficient decreases, which reduces the rate of particle transport from the bulk to the potential region. Also, the effect of drag force acting on the particle increases. As a result, the nanoparticle deposition and hence, K_D , k_{att} , and k_{det} decrease. This is also suggested by equations (36) and (37).

Theoretical [Hahn and O'Melia, 2004; Seetha *et al.*, 2014] and experimental studies [Compere *et al.*, 2001; Johnson *et al.*, 2007a; Knappett *et al.*, 2008; Kuznar and Elimelech, 2007; Li *et al.*, 2004, 2005; Litton and Olson, 1996; Sadeghi *et al.*, 2011; Shen *et al.*, 2007; Tosco *et al.*, 2012; Tufenkji and Elimelech, 2005; Wang *et al.*, 2012] have shown that the attachment rate coefficient increases with increasing solution ionic strength due to the compression of the electric double layers around the colloid and the collector, and the reduction in the negative surface potentials on the colloid and collector. Equations (36) and (37a) are in line with these findings as K_D and k_{att} show a negative trend with the surface potentials and a positive trend with the solution ionic strength. An opposite behavior is prescribed for k_{det} (equation (37b)). This is also consistent with the literature where decreasing values of detachment rate coefficient with increasing ionic strength for nano and micron-sized particles are observed [Compere *et al.*, 2001; Johnson *et al.*, 2007a; Li *et al.*, 2004, 2005].

As the average flow velocity increases, the diffusive flux toward the wall decreases, thus decreasing the nanoparticle deposition. Also, hydrodynamic drag force acting on the particles increases, resulting in increased particle mobilization in the potential region. Hence, K_D and k_{att} decrease (equations (36) and (37a)) and k_{det} (equation (37b)) increases with increasing v_m . This is in agreement with the column experimental results for colloids which show a negative trend between the colloid attachment rate coefficient and the pore water velocity [Hijnen *et al.*, 2005; Keller *et al.*, 2004; Li *et al.*, 2005; McKay *et al.*, 2002; Tong and Johnson, 2006]. Shen *et al.* [2010] did column experiments to study the transport of 30 nm latex microspheres through glass bead packed columns and found that the experimental collision efficiency decreased with increasing flow velocity. Torkzaban *et al.* [2007] did torque balance calculations around a spherical collector and found that the fraction of the collector surface area favorable for deposition (i.e., α) decreased with increasing velocity. Correlation equation of Tufenkji and Elimelech [2004a] predicts decreasing values of η_0 with increasing flow velocity and as a result, the attachment rate coefficient (based on CFT) decreases with increasing flow velocity. Tong and Johnson [2006] observed from column experiments that the attachment rate coefficient decreased and detachment rate coefficient increased with increasing the flow velocity

from 4 to 8 m/d for latex microsphere transport (size ranging from 100 nm to 2 μm) in soda-lime glass bead packed columns. Keller *et al.* [2004] conducted column-scale experiments to study the effect of transport velocity on the retention of MS2 and polystyrene beads of sizes 50 nm and 3 μm in sand, and observed that the effluent peak colloid concentration increased and the estimated attachment rate coefficient (and also the collision efficiency) decreased with increasing flow rate for all colloid sizes. Estimated values of detachment rate coefficient were found to increase [Seetha *et al.*, 2015] with increasing flow velocity for MS2 and ΦX174 transport in columns packed with glass beads [Syngouna and Chrysikopoulos, 2013]. Tosco *et al.* [2012] conducted column experiments to study the effect of flow velocity on the retention of 100 nm ferrihydrite particles under unfavorable conditions. They observed that the flow velocity has a significant effect on particle retention but only at high ionic strengths (5 and 10 mM). The particle deposition and the attachment rate coefficient were found to decrease with increasing flow velocity due to the greater effect of fluid drag on particle deposition in secondary minimum. Pore-scale studies conducted by May *et al.* [2012] in microfluidic flow cell packed with glass beads revealed that the nanoparticle retention decreased with increasing flow velocity. Li *et al.* [2005] studied the role of hydrodynamic drag on the deposition and reentrainment of 1.1 μm microspheres in porous media under unfavorable conditions. They found that the deposition rate coefficient decreased, and the detachment rate coefficient and the fraction of reversibly deposited colloids increased with increasing flow rate.

The effect of pore size on the deposition parameters depends on the relative significance of advection and diffusion, parameterized by Pe . For $Pe \leq 5$, diffusion is the dominant transport mechanism compared to advection and, nanoparticles near to the wall experience less hydrodynamic drag force with increasing pore radius. Hence, the equilibrium distribution coefficient increases with increasing pore radius (equation (36) and Tables 4–6). For $Pe > 5$, particle deposition onto the wall is restricted by advection and the radial diffusion length from the bulk region toward the wall increases with increasing pore radius. Hence, nanoparticle deposition decreases with increasing pore radius, resulting in decreasing k_{att} (equation (37a) and Tables 4–6) whereas k_{det} shows a nonmonotonic trend (equation (37b) and Tables 4–6). This result is consistent with Knappett *et al.* [2008], who conducted column experiments to study the effect of grain size on MS2 retention in angular sand, and found that decreasing the grain size from medium sand ($d_{50} = 0.7$ mm) to fine sand ($d_{50} = 0.34$ mm) resulted in 5-log reduction in MS2 effluent concentration and a correspondingly large attachment rate coefficient. Shen *et al.* [2008] conducted column experiments to study the transport of 30 and 66 nm carboxyl-modified polystyrene latex microspheres through glass bead columns under unfavorable conditions, and found that the deposition at both the primary and secondary minima contributed to the observed retention. They found that the attachment rate coefficients to both primary and secondary minima decreased with increasing the grain diameter from 0.11 to 0.72 mm. Ren *et al.* [2001] studied the effect of grain size on the deposition of 450 nm colloidal silica particles by performing column experiments. They observed that the effluent colloid concentration increased with increasing grain size. The experimental collision efficiency showed a negative correlation with the grain size, which indicates a negative correlation between attachment rate coefficient and the grain size as predicted by CFT. Though all columns were packed with the same bulk sand (but different grain sizes), the observed variation of collision efficiency with grain size was attributed to the variation of grain surface heterogeneity with grain size [Ren *et al.*, 2001]. Li *et al.* [2008] studied the nanoscale fullerene aggregate transport in saturated porous media and found that nanoparticle retention and the corresponding fitted attachment rate coefficient decreased as the grain size increased.

Tables 4–6 and equations (36) and (37) show that for $Pe \leq 5$, K_D follows a positive trend with nanoparticle radius whereas for $Pe > 5$, k_{att} and k_{det} follows a negative trend with nanoparticle radius. As diffusion is the dominant transport mechanism for $Pe \leq 5$, particle deposition depends on the favorability of the surfaces. As the secondary minimum depth and, hence, the surface favorability for deposition increases with increasing nanoparticle radius and the hydrodynamic drag is negligible, K_D increases with increasing nanoparticle radius (equation (36) and Tables 4–6). Advection becomes the dominant transport process for $Pe > 5$, and the nanoparticle diffusion coefficient decreases and hydrodynamic drag force acting on the particle near to the wall increases with increasing particle radius. Hence, k_{att} and k_{det} decrease with increasing nanoparticle radius (equation (37) and Tables 4–6). The trends described above are in line with the experimental observations from column experiments as explained below. Shen *et al.* [2008] conducted column experiments with various sizes of latex colloids and glass beads. They found that for a given size of glass bead collectors, the attachment rate coefficients of latex microspheres for both the primary and secondary minima are greater

for 30 nm colloids compared to the 66 nm colloids. *Tong and Johnson* [2006] studied the deposition and reentrainment behaviors of five sizes of microspheres (100 nm, 200 nm, 500 nm, 1 μm, and 2 μm) in porous media composed of soda lime glass beads in the presence of an energy barrier for deposition. The fitted attachment rate coefficient decreased, detachment rate coefficient increased, and the fraction of reversibly deposited colloids increased with increasing colloid size for particles below 1 μm at a pore water velocity of 4 m/d, though there was no clear trend at a pore water velocity of 8 m/d. In contrast, *Keller et al.* [2004] conducted column experiments to study the transport of MS2 (25 nm) and 50 nm polystyrene beads and observed that the attachment rate coefficient was greater for 50 nm colloids as compared to MS2. This might be due to the different surface characteristics of these two colloids. *Zvikelsky and Weisbrod* [2006] studied the impact of particle size on latex microsphere transport in fractured chalk cores and observed that the peak effluent colloid concentration increased with increasing colloid size from 20 to 200 nm. They found that diffusion is the dominant transport mechanism for all colloid sizes and the observed trend is due to the decreasing values of diffusion coefficient with increasing colloid size, which results in less transport to the fracture walls resulting in decreased deposition as well as penetration into the matrix. *Wang et al.* [2012] conducted column experiments to study the effect of nanoparticle size on their retention and transport in saturated porous media composed of Accusand. Silica nanoparticles, which are stable in a suspension, were selected as the representative nanoparticles with two different sizes of 8 and 52 nm. They observed that the retention was larger, with greater value of attachment rate coefficient for 8 nm particles than for 52 nm particles. Also, 100% of the deposited 8 nm sized particles and only 2% of the deposited 52 nm particles were released when flushing the column with low ionic strength solution after conducting experiments with 100 mM solution. This implies greater detachment for smaller particles, which is consistent with our pore-scale results. *Zhuang et al.* [2005] examined the size-dependent transport of amphiphilic latex colloids in saturated quartz sand columns. They observed that the transport of colloids was strongly particle size dependent. As the particle size increased from 20 to 420 nm, colloid deposition rate and the experimental collision efficiency first decreased to reach a minimum value at 100 nm, and then increased, indicating that different retention mechanisms were involved for nanoparticles (<100 nm) and colloids (>100 nm). This supports the results from our pore-scale model. *Shani et al.* [2008] studied the effect of particle size on colloid transport in natural dune sand by performing column experiments with 20 nm, 200 nm, and 1 μm colloids. They found that colloid retention decreased with increasing the colloid size from 20 to 200 nm and then increased thereafter. The dominance of diffusive transport and straining are the reasons for the greater retention of 20 nm and 1 μm colloids, respectively. They observed that the 200 nm particles were the most mobile.

7. Comparison With Colloid Filtration Theory

The correlation expression for the pore-scale attachment rate coefficient for the nanoparticles developed in this study (equation (37a)) can be qualitatively compared with the Darcy-scale colloid attachment rate coefficient ($k_{att(D)}$) predicted by CFT (equation (1)) under unfavorable conditions. For nanoparticles, diffusion is the dominant mechanism for transporting to the grain surface for deposition to occur [*Tufenkji and Elimelech*, 2004a; *Yao et al.*, 1971]. Hence, the single collector contact efficiency, η_0 , is approximately equal to the single collector efficiency due to diffusion (η_D). *Tufenkji and Elimelech* [2004a] derived a correlation equation for η_D by incorporating the influence of van der Waals attraction forces and hydrodynamic interactions on the diffusion mechanism and is given as

$$\eta_D \propto k_B^{0.663} T^{0.663} \mu^{-0.715} U^{-0.715} R^{-0.634} a^{-0.796} \tag{41}$$

Bai and Tien [1999] derived empirical expressions for the attachment efficiency of submicron and micron-sized colloids in porous media under unfavorable conditions using partial regression analysis and obtained a power law dependence of the experimental collision efficiency from column experiments with the various physicochemical parameters affecting it. The correlation equation of *Bai and Tien* [1999] is given as

$$\alpha \propto [N_A^{0.676} e^{1.352} k_B^{-0.676} \epsilon_0^{-0.9881}] \epsilon^{-0.9881} T^{-0.676} (\psi_1^2 + \psi_2^2)^{-0.3121} \rho^{0.676} \mu^{-0.391} U^{-0.391} a^{0.2579} \tag{42}$$

We neglected the effect of the parameter, N_{E2} in equation (42), to compare with our pore-scale expression. Substituting for η_D (equation (41)) and α (equation (42)) in equation (1) results in the following expression for colloid attachment rate coefficient at Darcy-scale under unfavorable conditions

$$k_{att(D)} \propto [N_A^{0.676} e^{1.352} k_B^{-0.013} \epsilon_0^{-0.9881}] \epsilon^{-0.9881} T^{-0.013} \mu^{-1.106} (\psi_1^2 + \psi_2^2)^{-0.3121} \rho^{0.676} U^{-0.106} R^{-1.634} a^{-0.5381} \tag{43}$$

Comparison of equation (37a) with equation (43) indicates that the trend predicted by equation (37a) for the parameters, ϵ , μ , $(\psi_1^2 + \psi_2^2)$, l , v_m , R , and a are consistent with equation (43) for the Darcy-scale attachment rate coefficient. However, $k_{att(D)}$ shows a downward trend with T , opposite to that predicted by k_{att} . Also, Darcy-scale attachment rate coefficient, $k_{att(D)}$, has been observed to increase with increasing T in experimental studies.

Elimelech [1992] used a semiempirical approach for predicting the attachment efficiency and obtained a power law relationship between the attachment efficiency and parameters characterizing the chemical-colloidal properties of the system. The corresponding expressions for α and $k_{att(D)}$ with η_D , expressed using Tufenkji and Elimelech [2004a] correlation equation, are given as

$$\alpha \propto [N_A^{0.595} e^{1.19} k_B^{-0.595} \epsilon_0^{-1.595}] \epsilon^{-1.595} T^{-0.595} \psi_1^{-1.19} \psi_2^{-1.19} \rho^{0.595} \tag{44}$$

$$k_{att(D)} \propto [N_A^{0.595} e^{1.19} k_B^{0.068} \epsilon_0^{-1.595}] \epsilon^{-1.595} T^{0.068} \mu^{-0.715} \psi_1^{-1.19} \psi_2^{-1.19} \rho^{0.595} U^{0.285} R^{-1.634} a^{-0.796} \tag{45}$$

Comparison of equations (37a) and (45) shows that except for v_m , the trends predicted by equation (37a) versus various parameters match with those obtained from equation (45). Elimelech [1992] assumed that α is affected only by the chemical-colloidal properties of the system (inverse Debye length, surface potentials on colloid and collector, and Hamaker constant) and hence $k_{att(D)}$ shows an increasing trend with v_m (equation (45)). This is in contrast to the observations from column experiments [Hijnen et al., 2005; Keller et al., 2004; Li et al., 2005; Shen et al., 2010; Tong and Johnson, 2006; Tosco et al., 2012] and pore-scale correlation equation (equation (37a)).

8. Conclusions

In this study, we have developed correlation equations for pore-scale averaged deposition coefficients for nanoparticles in a cylindrical pore under unfavorable conditions in terms of nine pore-scale parameters: the pore radius, nanoparticle radius, mean flow velocity, solution ionic strength, viscosity, temperature, solution dielectric constant, and nanoparticle and collector surface potentials. The correlation expressions are derived by performing a multiple-linear regression analysis between the deposition rate coefficients at pore-scale and the various pore-scale parameters. The data set for regression is created in two steps: (1) the advection-diffusion equation is solved for a cylindrical pore for a range of values of pore-scale parameters subject to a first-order reversible kinetic adsorption at the pore wall (the expressions for the mass transfer rate coefficients between the pore and the wall regions are derived in terms of the interaction energy profile) which accounts for the effect of nanoparticle-collector interaction forces on nanoparticle deposition, (2) the resulting BTCs and attached concentration curves obtained from the pore-scale model are fitted with 1-D advection-dispersion equation with an equilibrium or kinetic adsorption model, and the values of average deposition rate coefficients are calculated. Nanoparticle deposition at pore scale is best described by an equilibrium model at low Péclet numbers ($Pe = 0.05$) and a kinetic model at high Péclet numbers ($Pe = 50$). There exists an intermediate range (e.g., around $Pe = 5$), where both equilibrium and kinetic models can describe nanoparticle deposition. The correlation equations predict that the nanoparticle deposition at pore scale increases with increasing temperature and solution ionic strength, and it decreases with increasing solution viscosity, solution dielectric constant, nanoparticle and collector surface potentials, and flow velocity. Nanoparticle deposition is found to have a positive trend with pore radius and nanoparticle radius for $Pe \leq 5$, whereas a negative trend is predicted for $Pe > 5$. The correlation equations are found to be consistent with the observed trends from the column-scale and pore-scale experiments and, qualitatively agree with the colloid filtration theory under unfavorable conditions. These expressions can be incorporated into pore network models [Raouf et al., 2010], which represent porous media using an interconnected network of capillary pores. Using pore network model one can develop correlation equations for deposition rate coefficients at the Darcy scale in terms of measurable parameters such as the porosity, mean pore water velocity, mean pore radius, nanoparticle radius, solution ionic strength, viscosity, temperature, solution dielectric constant, and surface potentials of nanoparticle and grain surface.

Appendix A

A1. Diffusion Coefficients

Hydrodynamic wall effects retard particle diffusion in the diffusion and potential regions and also reduce the particle velocity. The position-dependent particle diffusion coefficients in the radial, D_{rr} , and axial directions, D_{zz} , and the velocity, v_2 , are given as [Seetha et al., 2014; Song and Elimelech, 1993]

$$D_{rr}(r) = f_1(r)D_\infty; \quad D_{zz}(r) = f_4(r)D_\infty; \quad v_2(r) = f_3(r) \frac{4v_m(R-r)}{R} \tag{A1}$$

Here f_1 and f_4 are, respectively, the universal hydrodynamic correction functions for the mobility of a freely moving particle perpendicular and parallel to the wall due to diffusion, and f_3 is the correction for particle velocity along the wall in simple shear flow, given by [Dahneke, 1974; Warszynski, 2000]

$$f_1(r) = \frac{R-r-a}{R-r} \tag{A2}$$

$$f_4(r) = \begin{cases} \left(\frac{\frac{R-r-a}{a}}{2.639 + \frac{R-r-a}{a}} \right)^{(1/4)} & ; R - \delta_D \leq r \leq R - 1.11a \\ \frac{1}{1.062 - 0.516 \ln \frac{R-r-a}{a}} & ; R - 1.11a < r \leq R - a \end{cases} \tag{A3a}$$

$$\tag{A3b}$$

$$f_3(r) = \begin{cases} 1 - \frac{0.304}{\left(1 + \frac{R-r-a}{a}\right)^3} & ; R - \delta_D \leq r \leq R - 1.137a \\ \frac{1}{0.754 - 0.256 \ln \left(\frac{R-r-a}{a}\right)} & ; R - 1.137a < r \leq R - a \end{cases} \tag{A4a}$$

$$\tag{A4b}$$

A2. Governing Equation in the Potential Region

Nanoparticle transport in the potential region is described by advection-diffusion equation in an interaction energy field [Seetha et al., 2014; Song and Elimelech, 1993; Wood et al., 2004]

$$\frac{\partial c}{\partial t} = \frac{\partial}{\partial r} \left(D_{rr} \frac{\partial c}{\partial r} \right) + \frac{1}{r} D_{rr} \frac{\partial c}{\partial r} + \frac{\partial}{\partial z} \left(D_{zz} \frac{\partial c}{\partial z} \right) + \frac{\partial}{\partial r} \left(\frac{D_{rr}}{k_B T} \frac{\partial \Phi}{\partial r} c \right) + \frac{1}{r} \frac{D_{rr}}{k_B T} \frac{\partial \Phi}{\partial r} c - v_2 \frac{\partial c}{\partial z}; \quad R - \delta_\varphi \leq r \leq R - a \tag{A5}$$

A3. Interaction Energy

The electrostatic double layer energy is calculated using HHF formula [Hogg et al., 1966] assuming constant surface potentials on nanoparticle and collector and is expressed as

$$\frac{\Phi_{EDL}}{k_B T} = N_{E1} \left[N_{E2} \ln \left(\frac{1 + e^{-(N_{DL} h^*)}}{1 - e^{-(N_{DL} h^*)}} \right) + \ln \left(1 - e^{-(2N_{DL} h^*)} \right) \right] \tag{A6}$$

Here $h^* = (h/a)$ is the dimensionless separation distance between the nanoparticle and the collector.

London-van der Waals interaction energy is calculated using the expression given by Gregory [1981] (equation (A7a)) for retarded sphere-plate interaction for $h^* \leq 0.2$ and Czarnecki's expression (equation (A7b)) [Gregory, 1981; Weroncki and Elimelech, 2008] for $h^* > 0.2$.

$$\frac{\Phi_{VDW}}{k_B T} = \frac{-H}{6h^* k_B T} \left[1 + \left(\frac{14h^*}{\lambda^*} \right) \right]^{-1}; \quad h^* \leq 0.2 \tag{A7a}$$

$$\frac{\Phi_{VDW}}{k_B T} = \frac{-H}{6k_B T} \left[\frac{2.45}{10\pi} \lambda^* p_1(h^*) - \frac{2.17}{120\pi^2} (\lambda^*)^2 p_2(h^*) + \frac{0.59}{840\pi^3} (\lambda^*)^3 p_3(h^*) \right]; \quad h^* > 0.2 \quad (A7b)$$

where the functions p_1 , p_2 , and p_3 are given by [Weronski and Elimelech, 2008]:

$$p_1(h^*) = \frac{1-h^*}{h^{*2}} + \frac{3+h^*}{(2+h^*)^2}; \quad p_2(h^*) = \frac{2-h^*}{h^{*3}} + \frac{4+h^*}{(2+h^*)^3}; \quad p_3(h^*) = \frac{3-h^*}{h^{*4}} + \frac{5+h^*}{(2+h^*)^4} \quad (A8)$$

Equation (A7b) is valid strictly for $h^* > (8/a)$. Hence, when this value becomes greater than 0.2, equation (A7a) needs to be used for $h^* \leq (8/a)$ and equation (A7b) for $h^* > (8/a)$ [Seetha et al., 2014].

Born potential energy is calculated using the formula derived by Ruckenstein and Prieve [1976] and is given below

$$\frac{\Phi_{Born}}{k_B T} = \frac{H(\sigma^*)^6}{7560k_B T} \left[\frac{8+h^*}{(2+h^*)^7} + \frac{6-h^*}{(h^*)^7} \right] \quad (A9)$$

Notation

a	nanoparticle radius [L].
a_0	radius of the nanoparticle-surface contact area [L].
A	interception parameter
c	nanoparticle number concentration in the pore [no. L ⁻³].
c_0	nanoparticle concentration at the pore inlet [no. L ⁻³].
c^*	dimensionless nanoparticle concentration.
\bar{c}^*	dimensionless nanoparticle breakthrough concentration.
c_u	courant number.
d_c	average grain diameter [L].
D	particle diffusion coefficient [L ² T ⁻¹].
Da_{att}, Da_{det}	Damköhler numbers corresponding to the rate coefficient for nanoparticle attachment to and detachment from the pore wall.
$Da_{ds}, Da_{sd}, Da_{sp}, Da_{ps}, Da_{dp},$ and Da_{pd}	Damköhler numbers corresponding to $k_{ds}, k_{sd}, k_{sp}, k_{ps}, k_{dp},$ and $k_{pd},$ respectively.
D_L	pore-scale dispersion coefficient [L ² T ⁻¹].
D_{rr}, D_{zz}	particle diffusion coefficients in the radial and axial directions in diffusion and potential regions [L ² T ⁻¹].
D_∞	particle bulk diffusion coefficient [L ² T ⁻¹].
e	elementary charge.
E	Young's modulus [M L ⁻¹ T ⁻²].
$f_1, f_2, f_3,$ and f_4	universal hydrodynamic correction functions.
f'_1, f'_2	fraction of particles in the primary minimum region and secondary minimum region that are mobile in the longitudinal direction by advection, respectively.
F_D	drag force acting on the nanoparticle [M L T ⁻²].
F_D^*	dimensionless function that accounts for the wall effects on fluid drag force.
h	separation distance between the nanoparticle and the wall [L].
h^*	dimensionless separation distance between the nanoparticle and the wall.
H	Hamaker constant [M L ² T ⁻²].
I	solution ionic strength [Molar].
J_h	particle flux in the radial direction in the potential region [no. L ⁻²].
k_B	Boltzmann constant [M L ² T ⁻² K ⁻¹].
k_{att}, k_{det}	average rate coefficients for nanoparticle attachment and detachment at pore scale [T ⁻¹].
$k_{att(D)}$	Darcy-scale attachment rate coefficient [T ⁻¹].
k_{ds}	mass transfer rate coefficient corresponding to nanoparticle transport from diffusion region to the secondary minimum region [LT ⁻¹].

k_{sd}	mass transfer rate coefficient corresponding to nanoparticle transport from secondary minimum region to the diffusion region [T^{-1}].
k_{sp}	mass transfer rate coefficient corresponding to nanoparticle transport from secondary minimum region to the primary minimum region [T^{-1}].
k_{ps}	mass transfer rate coefficient corresponding to nanoparticle transport from primary minimum region to the secondary minimum region [T^{-1}].
k_{dp}	mass transfer rate coefficient for nanoparticle transport from diffusion region to the primary minimum region [LT^{-1}].
k_{pd}	mass transfer rate coefficient for nanoparticle transport from primary minimum region to the diffusion region [T^{-1}].
K	composite Young's modulus [$M L^{-1} T^{-2}$].
K_D	equilibrium distribution coefficient [L].
K'_D	dimensionless equilibrium distribution coefficient.
l_H	lever arm [L].
L	length of cylindrical pore [L].
L^*	dimensionless length of the pore.
M_E	moment about the center of the particle created by fluid drag [$M L^2 T^{-2}$].
M_E^*	dimensionless function.
N_A	Avogadro number.
N_{E1}	dimensionless parameter representing the magnitudes of surface potentials.
N_{E2}	dimensionless parameter representing the ratio of surface potentials.
N_{DL}	dimensionless parameter representing the ratio of nanoparticle radius to double layer thickness.
Pe	Péclet number.
$Pe_{(1D)}$	1-D Péclet number.
r	radial coordinate [L].
r^*	dimensionless radial coordinate.
R	radius of cylindrical pore [L].
R_f	retardation factor.
\bar{s}_1, \bar{s}_2	average particle concentrations at primary and secondary minimum [no. L^{-2}].
\bar{s}^*	dimensionless average attached concentration.
\bar{s}_1^*, \bar{s}_2^*	dimensionless average particle concentration at primary and secondary minimum.
t	time [T].
t^*	dimensionless time.
t_{in}^*	duration of the input pulse (dimensionless).
T	absolute temperature [K].
T_A	adhesive torque acting on the particle [$M L^2 T^{-2}$].
T_H	hydrodynamic torque acting on the particle [$M L^2 T^{-2}$].
U	pore water velocity [$L T^{-1}$].
v_1	flow velocity in pore [$L T^{-1}$].
v_m	mean flow velocity in cylindrical pore [$L T^{-1}$].
\bar{v}_1	average velocity of mobile particles in the primary minimum region [$L T^{-1}$].
\bar{v}_2	average velocity of mobile particles in the secondary minimum region [$L T^{-1}$].
\bar{v}^*	average velocity of mobile particles.
z	axial coordinate [L].
z^*	dimensionless axial coordinate.
α	attachment efficiency.
η_0	single collector contact efficiency.
η_D	single collector efficiency due to diffusion.
δ_D	position of the interface between the bulk and diffusion regions measured from the surface of the pore [L].
δ_ϕ	position of the interface between the diffusion and potential regions measured from the surface of the pore [L].

$\delta s'$	distance from the collector surface beyond which particles are mobile in the secondary minimum region [L].
$\delta p'$	distance from the grain surface beyond which particles are mobile in the potential region [L].
Δt	time step [T].
Δz	step size [L].
ε	dielectric constant of water.
ε_0	permittivity of vacuum.
κ	inverse Debye-Huckel length [L ⁻¹].
λ	characteristic wavelength of the interaction [L].
λ^*	dimensionless parameter representing the ratio of characteristic wavelength of the interaction to nanoparticle radius.
μ	dynamic viscosity of water [M L ⁻¹ T ⁻¹].
ν	Poisson ratio.
Φ_{Born}	Born potential energy [M L ² T ⁻²].
Φ_{EDL}	electrostatic double layer energy [M L ² T ⁻²].
Φ_{VDW}	London-van der Waals energy [M L ² T ⁻²].
Φ^*	total dimensionless interaction energy.
ψ_1, ψ_2	surface potentials on the nanoparticle and collector.
σ	collision diameter [L].
σ^*	dimensionless parameter representing the ratio of collision diameter to nanoparticle radius.
θ	porosity.

Acknowledgments

The first author acknowledges a grant from Utrecht University for a 6 month visit to Netherlands. We thank J. F. Schijven (National Institute for Public Health and the Environment, Netherlands), S. A. Bradford (US Salinity Laboratory), and M. Th. van Genuchten (Federal University of Rio de Janeiro, Brazil) for very useful discussions. The candid review of the manuscript by C. V. Chrysikopoulos is greatly appreciated. His comments helped to improve the manuscript. The data used in this paper are generated by solving the governing equations given in sections 2 and 3. Data used to generate the figures in this paper can be accessed by contacting the corresponding author.

References

- Adamczyk, Z. (2006), *Particles at Interfaces: Interactions, Deposition, Structure, Interface Sci. Technol. Ser.*, vol. 9, Elsevier, Amsterdam, Netherlands.
- Anders, R., and C. V. Chrysikopoulos (2005), Virus fate and transport during artificial recharge recycled water, *Water Resour. Res.*, *41*, W0415, doi:10.1029/2004WR003419.
- Bai, R., and C. Tien (1999), Particle deposition under unfavorable surface interactions, *J. Colloid Interface Sci.*, *218*, 488–499, doi:10.1006/jcis.1999.6424.
- Barry, D. A., K. Bajracharya, M. Crapper, H. Prommer, and C. J. Cunningham (2000), Comparison of split-operator methods for solving coupled chemical nonequilibrium reaction/groundwater transport models, *Math. Comput. Simul.*, *53*, 113–127, doi:10.1016/S0378-4754(00)00182-8.
- Bergendahl, J., and D. Grasso (1999), Prediction of colloid detachment in a model porous media: Thermodynamics, *AIChE J.*, *45*(3), 475–484, doi:10.1002/aic.690450305.
- Bergendahl, J., and D. Grasso (2000), Prediction of colloid detachment in a model porous media: Hydrodynamics, *Chem. Eng. Sci.*, *55*, 1523–1532, doi:10.1016/S0009-2509(99)00422-4.
- Bradford, S. A., S. Torkzaban, and A. Wiegmann (2011), Pore-scale simulations to determine the applied hydrodynamic torque and colloid immobilization, *Vadose Zone J.*, *10*, 252–261, doi:10.2136/vzj2010.0064.
- Bradford, S. A., S. Torkzaban, and A. Shapiro (2013), A theoretical analysis of colloid attachment and straining in chemically heterogeneous porous media, *Langmuir*, *29*, 6944–6952, doi:10.1021/la4011357.
- Chang, Y. I., and H. C. Chan (2008), Correlation equation for predicting filter coefficient under unfavorable deposition conditions, *AIChE J.*, *54*(5), 1235–1253, doi:10.1002/aic.11466.
- Chrysikopoulos, C. V., and A. F. Aravantinou (2014), Virus attachment onto quartz sand: Role of grain size and temperature, *J. Environ. Chem. Eng.*, *2*, 796–801, doi:10.1016/j.jece.2014.01.025.
- Chu, Y., Y. Jin, M. Flury, and M. V. Yates (2001), Mechanisms of virus removal during transport in unsaturated porous media, *Water Resour. Res.*, *37*(2), 253–263, doi:10.1029/2000WR900308.
- Compere, F., G. Porel, and F. Delay (2001), Transport and retention of clay particles in saturated porous media. Influence of ionic strength and pore velocity, *J. Contam. Hydrol.*, *49*, 1–21, doi:10.1016/S0169-7722(00)00184-4.
- Dahneke, B. (1974), Diffusional deposition of particles, *J. Colloid Interface Sci.*, *48*(3), 520–522, doi:10.1016/0021-9797(74)90201-X.
- Derjaguin, B. V., and L. D. Landau (1941), Theory of the stability of strongly charged lyophobic sols and of the adhesion of strongly charged particles in solutions of electrolytes, *Prog. Surf. Sci.*, *43*, 30–59.
- Duffadar, R. D., and J. M. Davis (2008), Dynamic adhesion behavior of micrometer scale particles flowing over patchy surfaces with nano-scale electrostatic heterogeneity, *J. Colloid Interface Sci.*, *326*, 18–27, doi:10.1016/j.jcis.2008.07.004.
- Elimelech, M. (1992), Predicting collision efficiencies of colloidal particles in porous media, *Water Resour. Res.*, *26*(1), 1–8, doi:10.1016/0043-1354(92)90104-C.
- Elimelech, M., and C. R. O'Melia (1990), Kinetics of deposition of colloidal particles in porous media, *Environ. Sci. Technol.*, *24*, 1528–1536, doi:10.1021/es00080a012.
- Gasda, S. E., M. W. Farthing, C. E. Kees, and C. T. Millet (2011), Adaptive split-operator methods for modelling transport phenomena in porous medium systems, *Adv. Water Resour.*, *34*, 1268–1282, doi:10.1016/j.advwatres.2011.06.004.
- Goldman, A. J., R. G. Cox, and H. Brenner (1967), Slow viscous motion of a sphere parallel to a plane wall-II Couette flow, *Chem. Eng. Sci.*, *22*, 653–660, doi:10.1016/0009-2509(67)80048-4.

- Gregory, J. (1981), Approximate expressions for retarded van der Waals interaction, *J. Colloid Interface Sci.*, *83*(1), 138–145, doi:10.1016/0021-9797(81)90018-7.
- Hahn, M. W., and C. R. O'Melia (2004), Deposition and reentrainment of brownian particles in porous media under unfavorable chemical conditions: Some concepts and applications, *Environ. Sci. Technol.*, *38*, 210–220, doi:10.1021/es030416n.
- Hijnen, W. A. M., A. J. Brouwer-Hanzens, K. J. Charles, and G. J. Medema (2005), Transport of MS2 phage, Escherichia coli, Clostridium perfringens, Cryptosporidium parvum, and Giardia intestinalis in a gravel and a sandy soil, *Environ. Sci. Technol.*, *39*, 7860–7868, doi:10.1021/es050427b.
- Hogg, R., T. W. Healy, and D. W. Fuerstenau (1966), Mutual coagulation of colloidal dispersions, *Trans. Faraday Soc.*, *62*, 1638–1651.
- James, S. C., and C. V. Chrysikopoulos (2003), Effective velocity and effective dispersion coefficient for finite-sized particles flowing in a uniform fracture, *J. Colloid Interface Sci.*, *263*, 288–295, doi:10.1016/S0021-9797(03)00254-6.
- Johnson, K. L., K. Kendall, and A. D. Roberts (1971), Surface energy and the contact of elastic solids, *Proc. R. Soc. London, Ser. A*, *324*, 301–313.
- Johnson, P. R., N. Sun, and M. Elimelech (1996), Colloid transport in geochemically heterogeneous porous media: Modeling and measurements, *Environ. Sci. Technol.*, *30*, 3284–3293, doi:10.1021/es960053+.
- Johnson, W. P., X. Li, and S. Assemi (2007a), Deposition and re-entrainment dynamics of microbes and non-biological colloids during non-perturbed transport in porous media in the presence of an energy barrier to deposition, *Adv. Water Resour.*, *30*, 1432–1454, doi:10.1016/j.advwatres.2006.05.020.
- Johnson, W. P., M. Tong, and X. Li (2007b), On colloid retention in saturated porous media in the presence of energy barriers: The failure of α , and opportunities to predict η , *Water Resour. Res.*, *43*, W12513, doi:10.1029/2006WR005770.
- Kaluarachchi, J. J., and J. Morshed (1995), Critical assessment of the operator-splitting technique in solving the advection–dispersion–reaction equation: 1. Firstorder reaction, *Adv. Water Resour.*, *18*(2), 89–100, doi:10.1016/0309-1708(95)00001-Y.
- Keller, A. A., S. Sirivithayapakorn, and C. V. Chrysikopoulos (2004), Early breakthrough of colloids and bacteriophage MS2 in a water-saturated sand column, *Water Resour. Res.*, *40*, W08304, doi:10.1029/2003WR002676.
- Knappett, P. S., M. B. Emelko, J. Zhuang, and L. D. McKay (2008), Transport and retention of a bacteriophage and microspheres in saturated, angular porous media: Effects of ionic strength and grain size, *Water Res.*, *42*(16), 4368–4378, doi:10.1016/j.watres.2008.07.041.
- Kuznar, Z. A., and M. Elimelech (2007), Direct microscopic observation of particle deposition in porous media: Role of the secondary energy minimum, *Colloids Surf. A*, *294*(1–3), 156–162, doi:10.1016/j.colsurfa.2006.08.007.
- Li, X., T. D. Scheibe, and W. P. Johnson (2004), Apparent decreases in colloid deposition rate coefficients with distance of transport under unfavorable deposition conditions: A general phenomenon, *Environ. Sci. Technol.*, *38*, 5616–5625, doi:10.1021/es049154v.
- Li, X., P. Zhang, C. L. Lin, and W. P. Johnson (2005), Role of hydrodynamic drag on microsphere deposition and re-entrainment in porous media under unfavorable conditions, *Environ. Sci. Technol.*, *39*, 4012–4020, doi:10.1021/es048814t.
- Li, Y., Y. Wang, K. D. Pennell, and L. M. Abriola (2008), Investigation of the transport and deposition of fullerene (C60) nanoparticles in quartz sands under varying flow conditions, *Environ. Sci. Technol.*, *42*, 7174–7180, doi:10.1021/es01305y.
- Litton, G. M., and T. M. Olson (1996), Particle size effects on colloid deposition kinetics: Evidence of secondary minimum deposition, *Colloids Surf. A*, *107*, 273–283, doi:10.1016/0927-7757(95)03343-2.
- Loveland, J. P., J. N. Ryan, G. L. Amy, and R. W. Harvey (1996), The reversibility of virus attachment to mineral surfaces, *Colloids Surf. A*, *107*, 205–221, doi:10.1016/0927-7757(95)03373-4.
- Ma, H., M. Hradisky, and W. P. Johnson (2013), Extending applicability of correlation equations to predict colloidal retention in porous media at low fluid velocity, *Environ. Sci. Technol.*, *47*(5), 2272–2278, doi:10.1021/es304753r.
- May, R., S. Akbariye, and Y. Li (2012), Pore-scale investigation of nanoparticle transport in saturated porous media using laser scanning cytometry, *Environ. Sci. Technol.*, *46*, 9980–9986, doi:10.1021/es301749s.
- McKay, L. D., A. D. Harton, and G. V. Wilson (2002), Influence of flow rate on transport of bacteriophage in shale saprolite, *J. Environ. Qual.*, *31*, 1091–1105.
- Messina, F., D. L. Marchisio, and R. Sethi (2015), An extended and total flux normalized correlation equation for predicting single-collector efficiency, *J. Colloid Interface Sci.*, *446*, 185–193, doi:10.1016/j.jcis.2015.01.024.
- Nelson, K. E., and T. R. Ginn (2011), New collector efficiency equation for colloid filtration in both natural and engineered flow conditions, *Water Resour. Res.*, *47*, W05543, doi:10.1029/2010WR009587.
- O'Neill, M. E. (1968), A sphere in contact with a plane wall in a slow linear shear flow, *Chem. Eng. Sci.*, *23*, 1293–1298, doi:10.1016/0009-2509(68)89039-6.
- Park, Y., E. R. Atwill, L. Ho, A. I. Packman, and T. Harter (2012), Deposition of Cryptosporidium parvum Oocysts in porous media: A synthesis of attachment efficiencies measured under varying environmental conditions, *Environ. Sci. Technol.*, *46*, 9491–9500, doi:10.1021/es300564w.
- Putti, M., W. W. G. Yeh, and W. A. Mulder (1990), A triangular finite volume approach with high-resolution upwind terms for the solution of groundwater transport equations, *Water Resour. Res.*, *26*(12), 2865–2880, doi:10.1029/WR026i012p02865.
- Rajagopalan, R., and J. S. Kim (1981), Adsorption of brownian particles in the presence of potential barriers: Effect of different modes of double-layer interaction, *J. Colloid Interface Sci.*, *83*(2), 428–448, doi:10.1016/0021-9797(81)90339-8.
- Rajagopalan, R., and C. Tien (1976), Trajectory analysis of deep-bed filtration with the sphere-in-cell porous media model, *AIChE J.*, *22*(3), 523–533, doi:10.1002/aic.690220316.
- Raof, A., S. M. Hassanizadeh, and A. Leijnse (2010), Upscaling transport of adsorbing solutes in porous media: Pore-network modeling, *Vadose Zone J.*, *9*, 624–636, doi:10.2136/vzj2010.0026.
- Ratha, D. N., K. S. Hari Prasad, and C. S. P. Ojha (2009), Analysis of virus transport in groundwater and identification of transport parameters, *Pract. Period. Hazard. Toxic Radioact. Waste Manage.*, *13*(2), 98–109, doi:10.1061/(ASCE)1090-025X(2009)13:2(98).
- Ren, J., A. I. Packman, and C. Welty (2001), Analysis of an observed relationship between colloid collision efficiency and mean collector grain size, *Colloids Surf. A*, *191*, 133–144, doi:10.1016/S0927-7757(01)00770-1.
- Rodriguez, K., and M. Araujo (2006), Temperature and pressure effects on zeta potential values of reservoir minerals, *J. Colloid Interface Sci.*, *300*(2), 788–794, doi:10.1016/j.jcis.2006.04.030.
- Ruckenstein, E. (1978), Reversible rate of adsorption or coagulation of brownian particles-effect of the shape of the interaction potential, *J. Colloid Interface Sci.*, *66*(3), 531–543, doi:10.1016/0021-9797(78)90073-5.
- Ruckenstein, E., and D. C. Prieve (1973), Rate of deposition of brownian particles under the action of London and double-layer Forces, *J. Chem. Soc. Faraday Trans. 2*, *69*, 1522–1536.
- Ruckenstein, E., and D. C. Prieve (1976), Adsorption and desorption of particles and their chromatographic separation, *AIChE J.*, *22*(2), 276–283, doi:10.1002/aic.690220209.

- Sadeghi, G., J. F. Schijven, T. Behrends, S. M. Hassanizadeh, J. Gerritse, and P. J. Kleingeld (2011), Systematic study of effects of pH and ionic strength on attachment of phage PRD1, *Ground Water*, 49(1), 12–19, doi:10.1111/j.1745-6584.2010.00767.x.
- Seetha, N., M. S. Mohan Kumar, S. M. Hassanizadeh, and A. Raof (2014), Virus-sized colloid transport in a single pore: Model development and sensitivity analysis, *J. Contam. Hydrol.*, 164, 163–180, doi:10.1016/j.jconhyd.2014.05.010.
- Seetha, N., M. S. Mohan Kumar, and S. M. Hassanizadeh (2015), Modeling the co-transport of viruses and colloids in unsaturated porous media, *J. Contam. Hydrol.*, doi:10.1016/j.jconhyd.2015.01.002, in press.
- Shani, C., N. Weisbrod, and A. Yakirevich (2008), Colloid transport through saturated sand columns: Influence of physical and chemical surface properties on deposition, *Colloids Surf. A*, 316, 142–150, doi:10.1016/j.colsurfa.2007.08.047.
- Shen, C., B. Li, Y. Huiang, and Y. Jin (2007), Kinetics of coupled primary- and secondary-minimum deposition of colloids under unfavorable chemical conditions, *Environ. Sci. Technol.*, 41, 6976–6982, doi:10.1021/es070210c.
- Shen, C., Y. Huang, B. Li, and Y. Jin (2008), Effects of solution chemistry on straining of colloids in porous media under unfavorable conditions, *Water Resour. Res.*, 44, W05419, doi:10.1029/2007WR006580.
- Shen, C., Y. Huang, B. Li, and Y. Jin (2010), Predicting attachment efficiency of colloid deposition under unfavorable attachment conditions, *Water Resour. Res.*, 46, W11526, doi:10.1029/2010WR009218.
- Song, L., and M. Elimelech (1993), Calculation of particle deposition rate under unfavourable particle-surface interactions, *J. Chem. Soc. Faraday Trans.*, 89(18), 3443–3452, doi:10.1039/ft9938903443.
- Soraganvi, V. S., and M. S. Mohan Kumar (2009), Modeling of flow and advection dominant solute transport in variably saturated porous media, *J. Hydrol. Eng.*, 14(1), 1–14, doi:10.1061/(ASCE)1084-0699(2009)14:1(1).
- Spielman, L. A., and S. K. Friedlander (1974), Role of the electrical double layer in particle deposition by convective diffusion, *J. Colloid Interface Sci.*, 46(1), 22–31, doi:10.1016/0021-9797(74)90021-6.
- Syngouna, V. I., and C. V. Chrysikopoulos (2010), Interaction between viruses and clays in static and dynamic batch systems, *Environ. Sci. Technol.*, 44, 4539–4544, doi:10.1021/es100107a.
- Syngouna, V. I., and C. V. Chrysikopoulos (2013), Cotransport of clay colloids and viruses in water saturated porous media, *Colloids Surf. A*, 416, 56–65, doi:10.1016/j.colsurfa.2012.10.018.
- Tong, M., and W. P. Johnson (2006), Excess colloid retention in porous media as a function of colloid size, fluid velocity, and grain angularity, *Environ. Sci. Technol.*, 40, 7725–7731, doi:10.1021/es061201r.
- Torkzaban, S., S. M. Hassanizadeh, J. F. Schijven, H. A. M. de Bruin, and A. M. de Roda Husman (2006a), Virus transport in saturated and unsaturated sand columns, *Vadose Zone J.*, 5, 877–885, doi:10.2136/vzj2005.0086.
- Torkzaban, S., S. M. Hassanizadeh, J. F. Schijven, and H. H. J. L. van den Berg (2006b), Role of air-water interfaces on retention of viruses under unsaturated conditions, *Water Resour. Res.*, 42, W12514, doi:10.1029/2006WR004904.
- Torkzaban, S., S. A. Bradford, and S. L. Walker (2007), Resolving the coupled effects of hydrodynamics and DLVO forces on colloid attachment in porous media, *Langmuir*, 23, 9652–9660, doi:10.1021/la700995e.
- Tosco, T., J. Bosch, R. U. Meckenstock, and R. Sethi (2012), Transport of ferrihydrite nanoparticles in saturated porous media: Role of ionic strength and flow rate, *Environ. Sci. Technol.*, 46, 4008–4015, doi:10.1021/es202643c.
- Tufenkji, N., and M. Elimelech (2004a), Correlation equation for predicting single-collector efficiency in physicochemical filtration in saturated porous media, *Environ. Sci. Technol.*, 38, 529–536, doi:10.1021/es034049r.
- Tufenkji, N., and M. Elimelech (2004b), Deviation from the classical colloid filtration theory in the presence of repulsive DLVO interactions, *Langmuir*, 20, 10,818–10,828, doi:10.1021/la0486638.
- Tufenkji, N., and M. Elimelech (2005), Breakdown of colloid filtration theory: Role of the secondary energy minimum and surface charge heterogeneities, *Langmuir*, 21, 841–852, doi:10.1021/la048102g.
- Verwey, E. J. W., and J. T. G. Overbeek (1948), *Theory of the Stability of Lyophobic Colloids*, Elsevier, Amsterdam, Netherlands.
- Wang, C., A. D. Bobba, R. Attinti, C. Shen, V. Lazouskaya, L. Wang, and Y. Jin (2012), Retention and transport of silica nanoparticles in saturated porous media: Effect of concentration and particle size, *Environ. Sci. Technol.*, 46, 7151–7158, doi:10.1021/es300314n.
- Warszynski, P. (2000), Coupling of hydrodynamic and electric interactions in adsorption of colloidal particles, *Adv. Colloid Interface Sci.*, 84, 47–142, doi:10.1016/S0001-8686(99)00015-9.
- Weronksi, P., and M. Elimelech (2008), Novel numerical method for calculating initial flux of colloid particle adsorption through an energy barrier, *J. Colloid Interface Sci.*, 319, 406–415, doi:10.1016/j.jcis.2007.10.042.
- Wood, B. D., M. Quintard, and S. Whitaker (2004), Estimation of adsorption rate coefficients based on the Smoluchowski equation, *Chem. Eng. Sci.*, 59, 1905–1921, doi:10.1016/j.ces.2003.12.021.
- Yan, Z., X. Huang, and C. Yang (2015), Deposition of colloidal particles in a microchannel at elevated temperatures, *Microfluidics Nano-fluidics*, 18(3), 403–414, doi:10.1007/s10404-014-1448-1.
- Yao, K. M., M. T. Habibian, and C. R. O'Melia (1971), Water and waste water filtration: Concepts and applications, *Environ. Sci. Technol.*, 5(11), 1105–1112, doi:10.1021/es60058a005.
- Zhang, Q. (2013), Colloid transport, retention, and remobilization during two-phase flow, PhD thesis, Dep. of Earth Sci., Utrecht Univ., Utrecht, Netherlands.
- Zhang, Q., S. M. Hassanizadeh, N. K. Karadimitriou, A. Raof, B. Liu, P. J. Kleingeld, and A. Imhof (2013), Retention and remobilization of colloids during steady-state and transient two-phase flow, *Water Resour. Res.*, 49, 8005–8016, doi:10.1002/2013WR014345.
- Zhang, Q., S. M. Hassanizadeh, B. Liu, J. F. Schijven, and N. K. Karadimitriou (2014), Effect of hydrophobicity on colloid transport during two-phase flow in a micromodel, *Water Resour. Res.*, 50, 7677–7691, doi:10.1002/2013WR015198.
- Zhuang, J., and Y. Jin (2003), Virus retention and transport as influenced by different forms of soil organic matter, *J. Environ. Qual.*, 32, 816–823, doi:10.2134/jeq2003.8160.
- Zhuang, J., J. Qi, and Y. Jin (2005), Retention and transport of amphiphilic colloids under unsaturated flow conditions: Effect of particle size and surface property, *Environ. Sci. Technol.*, 39, 7853–7859, doi:10.1021/es050265j.
- Zvikelsky, O., and N. Weisbrod (2006), Impact of particle size on colloid transport in discrete fractures, *Water Resour. Res.*, 42, W12508, doi:10.1029/2006WR004873.